

ÉCOLE POLYTECHNIQUE
MASTER: HEP PHYSICS MASTER
KLEIMENOV Maksim

RAPPORT DE STAGE DE RECHERCHE

**«Modèle lepto-hadronique de microquasars galactiques
expliquant les observations de rayons gamma à ultra-haute énergie»**

(«Lepto-hadronic model of Galactic microquasars
explaining ultra-high energy gamma-ray observations»)

RAPPORT NON CONFIDENTIEL

Option : Département de Physique

Champ : Astrophysique et Cosmologie

Enseignant référent : Alain Lecavelier des Étangs

Tuteur de stage dans l'organisme : Dmitri Semikoz

Dates du stage: 24/03/2025 – 18/07/2025

Adresse de l'organisme : 85 Boulevard Saint-Germain 75006 Paris France

Déclaration d'intégrité relative au plagiat

Je soussigné Kleimenov Maksim certifie sur l'honneur :

1. Que les résultats décrits dans ce rapport sont l'aboutissement de mon travail.
2. Que je suis l'auteur de ce rapport.
3. Que je n'ai pas utilisé des sources ou résultats tiers sans clairement les citer et les référencer selon les règles bibliographiques préconisées.

Je déclare que ce travail ne peut être suspecté de plagiat.

Date

...30/06/2025...

Signature

A handwritten signature in blue ink, appearing to read "Maksim Kleimenov".

Abstract

Nous présentons une étude de la nébuleuse de rayons gamma de très haute énergie récemment détectée par HAWC, LHAASO et H.E.S.S. autour du microquasar V4641 Sgr, l'un des plus violents connus. Après une brève revue observationnelle de la source et de son environnement, nous développons et testons plusieurs modèles leptoniques et hadroniques visant à expliquer les caractéristiques spectrales et morphologiques de la nébuleuse. En supposant que les particules chargées se propagent le long des lignes de champ magnétique galactique, nous modélisons le transport par diffusion et simulons la transition entre les régimes balistique et diffusif à l'aide de l'équation du télégraphiste. Parmi les scénarios leptoniques, nous privilégions un modèle à injection continue d'électrons, initiée il y a plusieurs milliers d'années, avec un champ magnétique d'intensité supérieure à $2 \mu\text{G}$. L'asymétrie observée de la nébuleuse est alors attribuée soit à la courbure des lignes de champ régulières, soit à la transition balistique-diffusive le long d'un champ incliné. Un modèle purement hadronique à flash unique ne parvenant pas à reproduire le flux de rayons X observé, nous construisons deux scénarios hybrides lepto-hadroniques impliquant respectivement une injection électronique impulsive ou continue. Dans ces cas, l'asymétrie est naturellement expliquée par l'inhomogénéité du gaz environnant. Enfin, nous suggérons que des mesures futures dans le domaine des rayons X durs et des neutrinos permettront de discriminer les différents scénarios proposés.

Abstract

We present a study of the ultra-high-energy gamma-ray nebula recently detected by HAWC, LHAASO, and H.E.S.S. around the violent microquasar V4641 Sgr. After a concise observational review of the source and its environment, we develop and test several leptonic and hadronic models to explain both the spectral and morphological characteristics of the nebula. Assuming charged particle propagation along the Galactic magnetic field lines, we model particle transport via diffusion and simulate the transition from ballistic to diffusive regimes using the telegrapher's equation. Among leptonic scenarios, we favor a continuous electron injection model initiated several thousand years ago, with a magnetic field strength exceeding $2 \mu\text{G}$. The observed asymmetry of the nebula is then attributed either to bending of regular magnetic field lines or to the ballistic-diffusive transition along an inclined magnetic field. As a purely hadronic single-flash model fails to reproduce the observed X-ray flux, we construct two hybrid lepto-hadronic models involving either a flash-like or continuous electron injection. In these cases, the asymmetry is naturally explained by the inhomogeneous gas distribution near the source. Finally, we propose that future measurements in the hard X-ray and neutrino domains will help distinguish between the competing scenarios.

Contents

Introduction	4
1 The Microquasar V4641 Sgr	5
1.1 Observational review	5
1.2 The Binary System	8
1.3 Galactic Bar	10
1.4 Surroundings of the Source	11
1.5 Extended radiation from the source: X-Ray to Gamma	12
2 Cosmic Ray Transport	15
2.1 General remarks	15
2.2 Ballistic regime	16
2.3 Diffusive regime	16
2.4 Ballistic-Diffusive transition	18
3 Leptonic model	20
3.1 Interactions and Timescales	20
3.2 Single Flare Scenario	23
3.3 Constant Emission Diffusive Scenario	25
3.4 Constant Emission Ballistic Transition Scenario	27
4 Hadronic Mechanism	29
4.1 Interactions and Timescales	29
4.2 HI4PI Hydrogen Maps	30
4.3 Proton Flash Scenario	32
4.4 Proton-Electron Flash	33
4.5 Proton Flash and Electron Emission	35
5 Results and Discussion	37
References	39
Appendices	42
A Solving the Diffusion Equation	42
B Cosmic-Ray Diffusion in QLT	45
C Cosmic-Rays Propagation and Telegrapher's Equation	47
D Solving the Transport Equation	49
E Inverse Compton and Synchrotron Radiation	52
F Cold proton density and hadronic emission	52
G Rescaling XRISM X-ray measurements	52
H Measuring orthogonal diffusion coefficient	52

Introduction

Since Victor Hess's 1912 balloon experiments revealed the existence of cosmic rays (CRs), their origin has remained one of the central open questions in high-energy astrophysics. Despite over a century of observational and theoretical efforts, the mechanisms and sources responsible for accelerating particles to PeV energies are still under active investigation, particularly within our Galaxy.

The cosmic ray (CR) spectrum extends from several GeV up to ultra-high energies (UHE). Detailed measurements have shown that the CR spectrum spans from a few GeV to ultra-high energies (UHE). Though roughly a power law, several distinct features appear: a steepening of the index from 2.7 to 3.1 at $3 \cdot 10^{15}$ eV (the *knee*), a flattening near $4 \cdot 10^{18}$ eV (the *ankle*), and a suppression around 10^{20} eV (the *GZK cutoff*) [1]. While supernova remnants and pulsar wind nebulae can plausibly explain CRs up to the knee, particles above this energy likely require more powerful—or even exotic—accelerators. Since UHECRs are thought to originate from extragalactic sources, the region between the knee and the ankle is often interpreted as a transition zone from galactic to extragalactic CRs. This has led to an active search for galactic *PeVatrons*: sources capable of accelerating hadrons beyond 1 PeV [2].

A promising class of candidates is *microquasars* (MQs)—binaries consisting of a star and a compact object (black hole or neutron star) that produces relativistic jets. First identified with SS 433 in 1979, around 20 MQs are now known in the Milky Way.

Recent advances in gamma-ray astronomy, particularly the development of imaging atmospheric Cherenkov telescopes (H.E.S.S., MAGIC, VERITAS, and the forthcoming CTAO) and extensive air shower arrays (HAWC, LHAASO), have enabled the detection of high-energy gamma-ray emission from several microquasars, including SS 433 and Cygnus X-3 [3]. These discoveries have renewed interest in the search for hadronic interaction signatures in compact binary systems. Interpreting the complex, multimessenger signals from such sources remains a central challenge in high-energy astrophysics.

In 2024, HAWC, LHAASO and H.E.S.S. reported detection of a ~ 100 pc HE nebula associated with the microquasar V4641 Sgr [4, 5, 6]. This system is famous for its violent 1999 X-Ray burst followed by a superluminous radio jet [7, 8]. With its combination of moderately extended X-ray emission [9] and extreme gamma-ray energies reaching 800 TeV, this source has emerged as a natural candidate for cosmic-ray production above the knee.

In this work, we develop leptonic and hadronic models to fit multiwavelength observations. Section 1 reviews current knowledge of V4641 Sgr; section 2 overviews ballistic and diffusive cosmic-ray transport and introduces a simple transition model. Section 3 presents three leptonic scenarios: one single-flash and two continuous emission cases. In section 4, we introduce three hadronic models: a proton-flash only, a lepto-hadronic flash, and a proton flash with continuous electron emission. We conclude with a discussion of results and propose new observables to distinguish among the models in section 5. The main text is followed by appendices detailing the mathematical and computational methods used.

1. The Microquasar V4641 Sgr

V4641 Sgr is a low-mass X-ray binary (LMXB) located close to λ Sagittarii (Figure 1), approximately 8° from the Galactic Center (Table 1). Having been under multi-wavelength observation since its dramatic X-ray outburst in 1999, the source exhibits regular short-lived flares. In 2024, V4641 Sgr was found to be surrounded by a gamma-ray nebula emitting photons up to 1 PeV.

J2000 (α, δ)	$18^{\text{h}} 19^{\text{m}} 22^{\text{s}}$	$-25^\circ 24' 25''$
J2000 (α, δ)	274.840	-25.407
Galactic (l, b)	6.774	-4.789

Table 1: *Coordinates of the V4641* derived from the Gaia Data Release 3 [10, 11] in equatorial (J2000) and galactic frames.

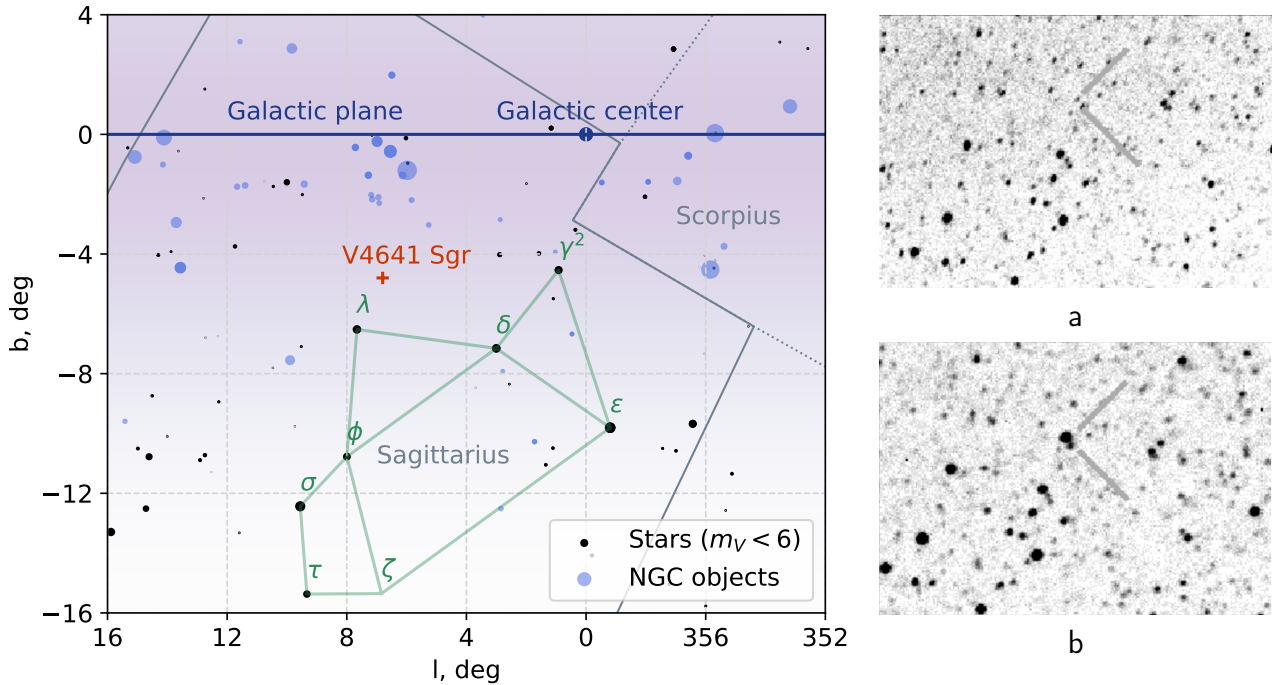


Figure 1: *Left:* A skymap of the Sagittarius constellation in Galactic coordinates, with the teapot asterism outlined in green. Constellation boundaries are shown in grey, and the Galactic plane is indicated in blue. The blue point at $(0, 0)$ marks the Galactic center. V4641 Sgr is indicated by a red cross. Positions were retrieved from the VizieR catalogues V/50 (Hipparcos) [12, 13], and VII/118 (SIMBAD) [11], accessed via astroquery [14].

Right: Optical images taken with a 25-cm Schmidt–Cassegrain telescope at Kyoto University [15]. Panels a and b were captured on September 9 and September 15, 1999, respectively.

1.1. Observational review

The first observation of V4641 Sgr was made by Goranskij at $m_V = 12.2$ in 1978, who misidentified it as *GM Sgr*, a Mira-type star known since 1927. Activity of this binary system between 1960 and 1992 has since been revealed through the analysis of photographic plates archived at the Sternberg Astronomical Institute in Moscow, Russia, and at the Sonneberg Observatory in Sonneberg, Germany [16]. In early 1999, the source was detected in the X-ray band as SAX J1819.3–2525.

Major Outburst in September 1999: from Radio to X-Ray

On September 15, 1999, Rob Stubbings, an amateur astronomer from Australia, *visually* detected a dramatic optical outburst of the source, reaching a magnitude of $m_V = 8.8$ [17]. The alert he issued was confirmed by Kyoto University (Figure 1a,b) and subsequently forwarded to the Rossi X-ray Timing Explorer (RXTE) and the Very Large Array (VLA) in the USA [18]. The maximum flux registered from the star reached 12.2 Crab. Very-long-baseline interferometry (VLBI) observations revealed a large-scale *superluminal jet* emerging from the source (Figure 2). This outburst was also observed by ATCA, MERLIN, RATAN, GBI, and MOST at various radio frequencies [7].

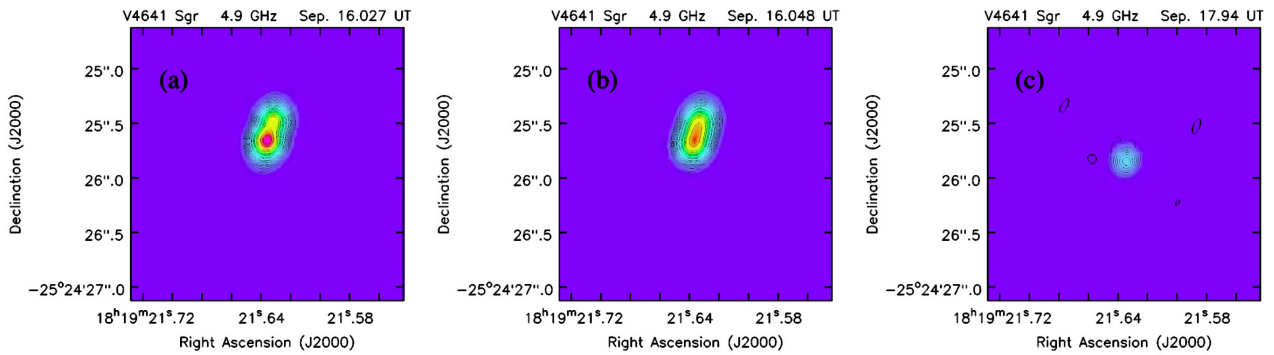


Figure 2: VLBI picture [7] with an overlaid color pattern [19].

a) September 16.027 UT; b) September 16.048 UT; c) September 17.94 (~ 2 days difference).

Further Observations

After 1999, visual outbursts became more frequent. One flare recorded in the 20th century was an outburst in 1978, which led to a detailed investigation of the star [16]. Figure 3 shows historical lightcurve of the source in visible (V) and blue (B) optical bands. The flares are distinct: some of them appear in all three domains (2002, 2003, 2004); some are radio-quiet (2005, 2007, 2015, 2018, 2020, 2021) [20].

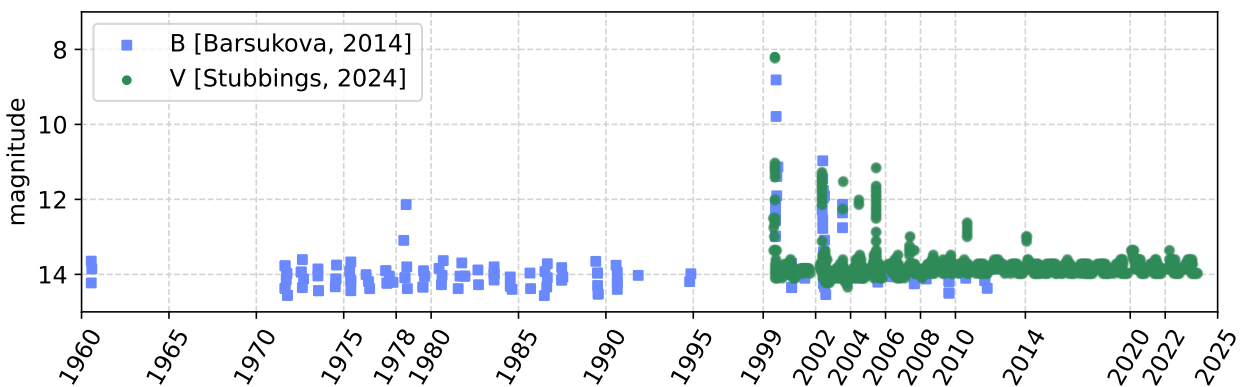


Figure 3: Historical lightcurve of the V4641 Sgr in blue [16], and visible [18] bands.

As with other LMXBs, V4641 Sgr spends most of its time in the *quiescent state*, during which the luminosity is dominated by the companion star. A meticulous investigation of quiescence by [21] identifies two distinct phases: a *passive state*, comprising approximately 85% of the quiescent period and characterized by stable brightness modulated by orbital variations; and an *active state*, covering the remaining 15%, which is both brighter and more variable than the passive one.

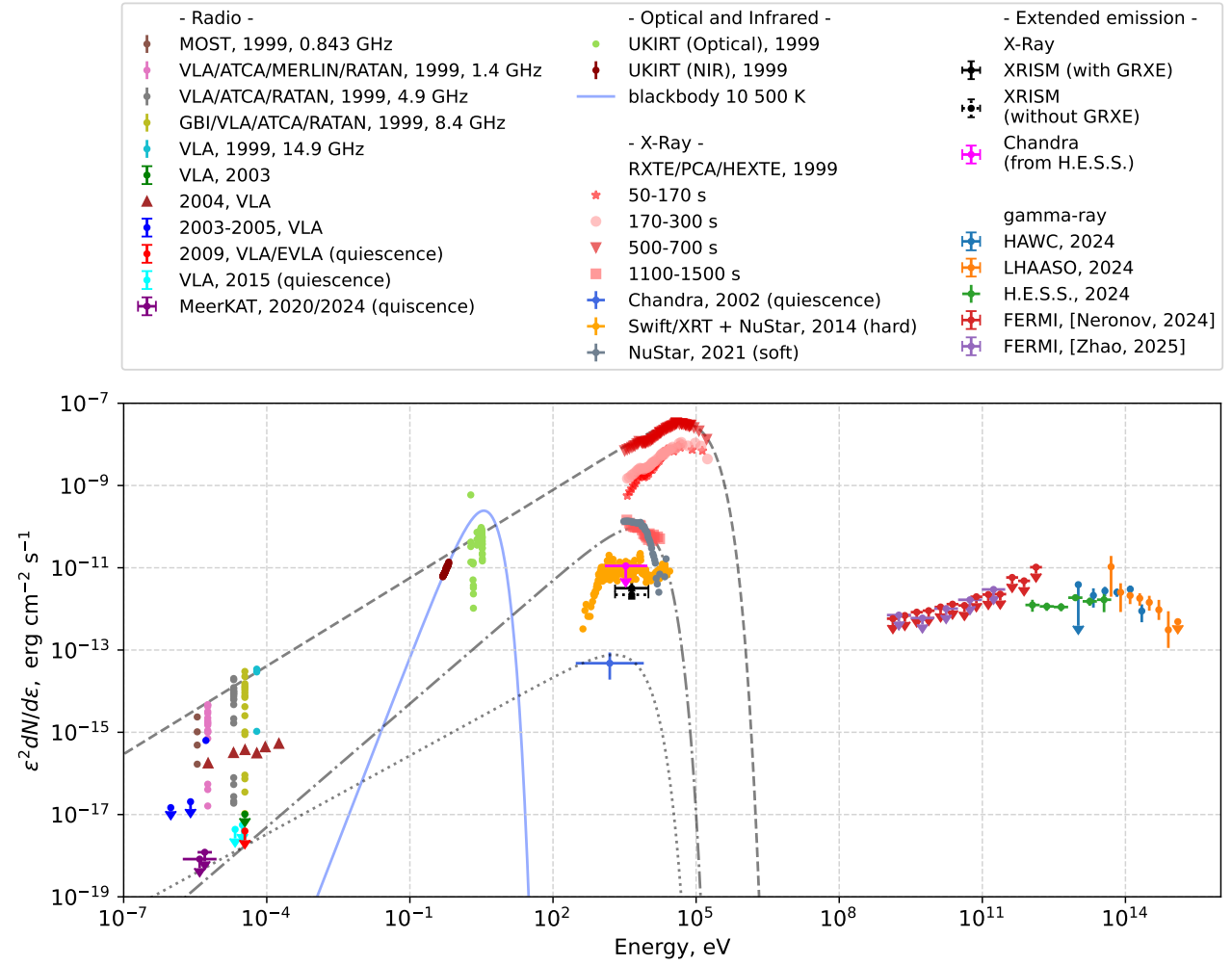


Figure 4: *Combined broad-band measurements of the V4641 X-ray binary and its nebula.*

Point-source observations: *Radio measurements* were taken in 1999 [7] and 2004 (#296 from [20]), with upper limits reported in 2003-2005 [22], 2009 [23], 2015, 2020 and 2024 (#7908, #13471, #16852 from [20] respectively).

Infrared and optical data from the 1999 outburst are available in [24], blackbody radiation curve is drawn for $T = 10\,500$ K [25].

X-ray observations have been primarily conducted by NuSTAR [26] and Swift [27], with a key measurement of the 1999 flash provided by [8]. X-Ray flux in quiescence is registered with Chandra [28]

Extended region measurements: *Gamma-ray observations* were carried out in 2024 by H.E.S.S. [6], HAWC [4], and LHAASO [5]. Upper limits in the GeV range are based on FERMI [29, 30].

X-Ray upper-limit is set by H.E.S.S. from Chandra [6], extended emission is measured by XRISM with and without GRXE [9].

When relevant, the values were rescaled with the use of $d = 6.1$ kpc.

Component	Luminosity, erg s ⁻¹	L/L_{Ed}	lifetime	Energy, erg
Quiescence	10^{33}	$\sim 10^{-6}$	1 yr	$3 \cdot 10^{43}$
Companion star	$4 \cdot 10^{35}$	$5 \cdot 10^{-3}$	1 yr	$1.4 \cdot 10^{43}$
'Hard' state	10^{35}	$\sim 10^{-4}$	1 day	10^{43}
'Soft' state	10^{36}	$\sim 10^{-3}$	1 day	10^{44}
1999 flare [8]	$5 \cdot 10^{38}$	0.63	1 h	$2 \cdot 10^{42}$
1999 flare [31]	$1.3 \cdot 10^{39}$	1.6	100 s	10^{41}
UHE component	$5 \cdot 10^{34}$	$6 \cdot 10^{-5}$	1 yr	$2 \cdot 10^{45}$

Table 2: Luminosities, characteristic lifetimes and energies corresponding to different components of the observed radiation from the system. In the third column values are compared to Eddington luminosity of a $6.4M_{\odot}$ black hole $L_{\text{Ed}} = 8 \cdot 10^{38}$ erg s⁻¹. The peak luminosity of the 1999 flare is reported in [31] to be 12.2 Crab = $3 \cdot 10^{-7}$ erg cm² s⁻¹.

Rare and short-lived outbursts, occurring approximately once per year and lasting up to several days, exhibit a variety of spectral patterns. These are typically classified into *soft* and *hard* states, depending on whether the X-ray spectrum is dominated by thermal emission from the accretion disk or by a power-law component [26].

Observations of flares, along with several quiescence fluxes and upper limits, are shown in Figure 4 (see caption for references). To estimate energetics of low-energy signal from the binary, we plotted three profiles to fit the observations: a dashed gray curve for the 1999 flare, a dash-dotted for the 'soft' state of the source and a dotted one for a quiescent state. Approximate luminosities are gathered in

1.2. The Binary System

Detailed investigations of the binary system conducted since 1999 have placed significant constraints on the parameters of its constituents. The most recent measurements are summarized in Table 3.

Initially estimated at 0.5 kpc in 2000 based on neutral hydrogen absorption spectra [7], the distance to the system has gradually converged to an average value of 6.1 ± 0.5 kpc (Figure 5). In 2001, photometric estimates suggested a range of $7.40 < d < 12.31$ kpc [25], while a subsequent study in the optical and near-infrared (NIR) domains two years later constrained the distance to $3 < d < 8$ kpc [24]. In 2014, multiparametric modeling of the eclipse light curve yielded $d = 6.2 \pm 0.7$ kpc [21], a result later supported by astrometric observations from the second and third Gaia data releases [34, 10].

	Measured value	Ref.
d	6.1 ± 0.5 kpc	Fig. 5
α	$274^{\circ}.8401 \pm 0.0204$	
δ	$-25^{\circ}.4072 \pm 0.0185$	[10]
$\dot{\alpha}$	-0.78 ± 0.03 mas/yr	
$\dot{\delta}$	0.43 ± 0.02 mas/yr	
v_{rad}	72.7 ± 3.3 km/s	[32]
M_{BH}	$6.4 \pm 0.6 M_{\odot}$	
a	$17.5 \pm 1.0 R_{\odot}$	[21]
P	2.817 ± 0.002 d	
i	$72.3 \pm 4.1^{\circ}$	
M_{\star}	$2.9 \pm 0.4 M_{\odot}$	[21]
R_{\star}	$5.3 \pm 0.3 R_{\odot}$	
T_{eff}	$10\,500 \pm 300$ K	[25]
v_{jet}	$> 0.990c$	[33]
α_{jet}	$< 16^{\circ}$	
l_{jet}	$\sim 10^{-3}$ pc	Fig. 2

Table 3: Parameters of the binary.

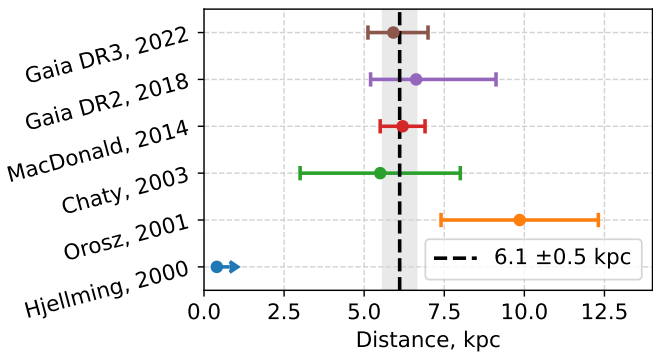


Figure 5: V4641 distance measurements based on spectroscopy [25, 24, 21] and astrometry [34, 10].

This distance revision increases the jet velocities inferred in 2000 from $1.0c < v < 3.2c$ to $7.9c < v < 39c$, corresponding to $v_{jet} > 0.990c$, $\alpha_{jet} < 16^\circ$, and justifying the classification of V4641 as a “microblazar” [33]. These measurements are further supported by the absence of $H\alpha$ emission lines in the observed spectrum [24].

It is important to note that, due to this long-standing uncertainty in distance estimates, luminosity values reported in earlier studies should be interpreted with caution.

The companion star to the $6.4 M_\odot$ black hole has a mass of $2.9 M_\odot$ and is classified as a B9III-type giant with temperature of 10 250 K [25, 21]. Geometry of the system is well-constrained from the X-Ray eclipse data.

There is evidence of an accretion disk in the system, however its properties are weakly constrained. Optical and NIR measurements are consistent with a non-relevant accretion disc with $T \sim 5000$ K [21]; X-Ray measurements prefer $T = 1.14 \pm 0.03$ eV ~ 13 MK and $i_{disk} = 43 \pm 15^\circ$ [36].

A low-luminosity accretion disc wind with terminal velocity $900 \text{ km/s} < u < 1600 \text{ km/s}$ was detected from the binary during its major outbursts [37]. In 1999, the wind speed could be up to 3 000 km/s.

A schematic summary of the binary system geometrical properties is shown in Figure 6.

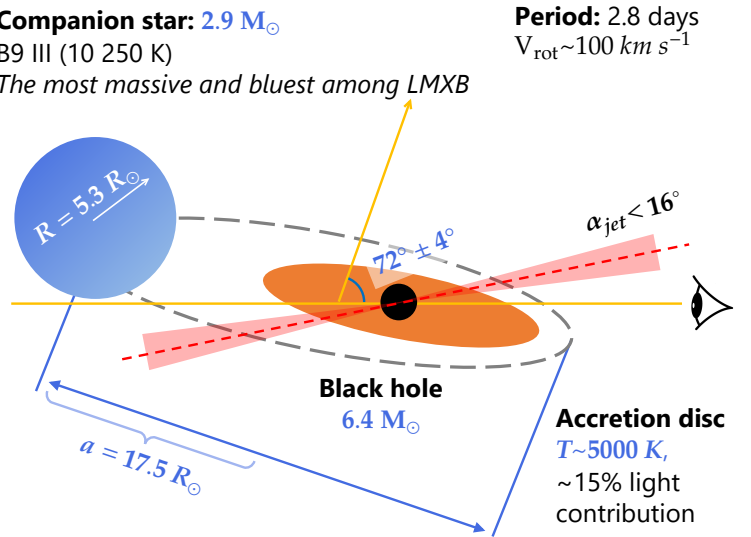


Figure 6: Geometric properties of the binary [21, 25, 35].

1.3. Galactic Bar

Central region of the Milky Way

Current position of the source is rather peculiar. Its galactocentric coordinates are $(-2.1, 0.7, -0.5)$ kpc for $d = 6.1$ kpc, which means that it is located in the vicinity of the *Galactic Bar*.

Galactic bar is a non-axisymmetric vertically extended stellar over-density region in the Milky Way center. The bar is usually split into two parts: *boxy/peanut bulge* (dark green in Figure 7), which is localized in a box of size $(\pm 2.2 \times \pm 1.4 \times \pm 1.2)$ kpc [38], and a *long bar*, which is a thin $h \sim 180$ pc elongated $a \sim 4$ kpc ellipsoid-like structure in the Galactic plane [39] (drawn with light-green in Figure 7). Stellar density profiles in the bar decay exponentially from the galactic center; by "size" here we mean characteristic scales of the function in the corresponding exponent.

Major axis of the bar is inclined at the angle of 27° to the axis, which connects the Sun and the Galactic Center [40].

In terms of stellar kinematics, the stars in the bar stand out from common galactic-disk stars: the bar rotates as a solid body, when galactic dist has almost a constant rotation curve up to ~ 2 kpc [41]. Angular velocity estimations of the bar rotation converge to a value $\Omega_b \approx 40$ km/s kpc $^{-1}$ [42]. This means, that the stars and gas in the bar behave differently from the ones in galactic disk.

Within the distance measurement errors, V4641 Sgr can be situated both inside, and outside the bar structure, which allows for a significant variations of Galactic medium properties near the binary.

Astrometric and spectroscopic measurements of the binary [10, 32] allow to define the movement direction of V4641. Figure 7 shows three velocity vectors for the source: relative to the Sun (gray), to the Galactic Center (black), and to the Bar assuming $\Omega_b = 40$ km/s kpc $^{-1}$, $d = 6.1$ kpc, $d_\odot = 8.12$ kpc. The calculations were made with the astropy library in Python 3 [43].

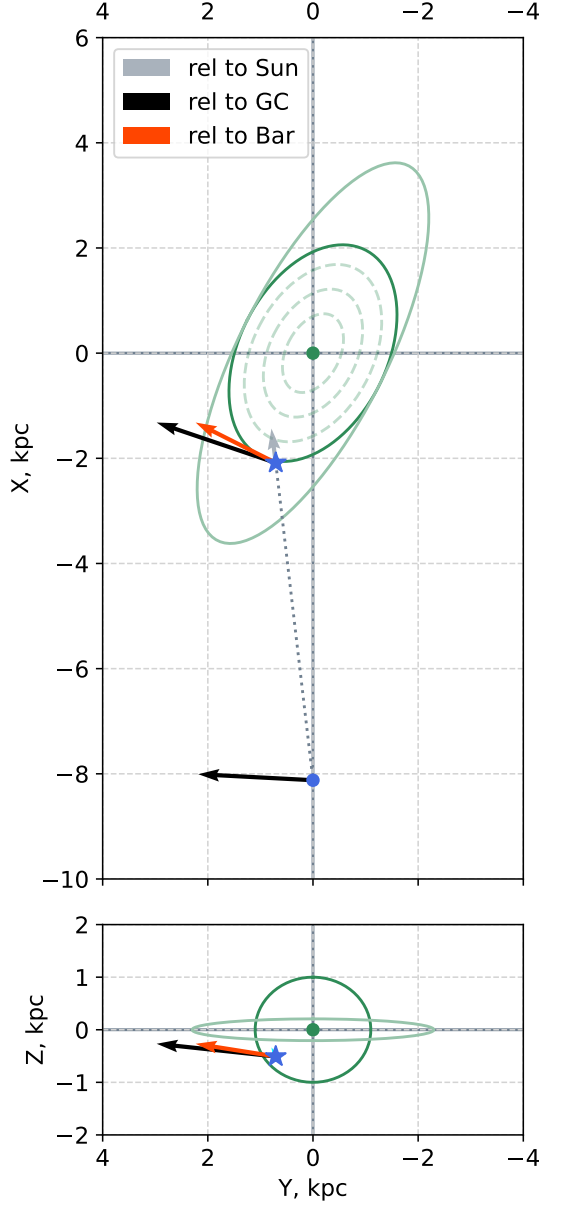


Figure 7: V4641 (blue star) and the Sun (blue dot) in galactocentric frame with their velocities relative to the Sun (gray), to GC (black), to the Bar (red).

1.4. Surroundings of the Source

Photon background

The source is floating in the low-energy radiation field, which consists of cosmic microwave background (CMB) and Interstellar Radiation Field (ISRF) represented by Starlight coming from all the Galaxy, and thermal radiation from the dust, which reemits absorbed optical photons in infrared (IR) diapason. Extragalactic radiation (EBL) contribution is negligible in comparison to galactic components in optical and IR. Density and energy-density profiles of background are calculated from an axisymmetric model [44].

The proximity of the source to the Bar can result into an increase in stellar and dust components of the background radiation. As we show in the following chapters, this will not contribute significantly to the gamma-ray spectrum description.

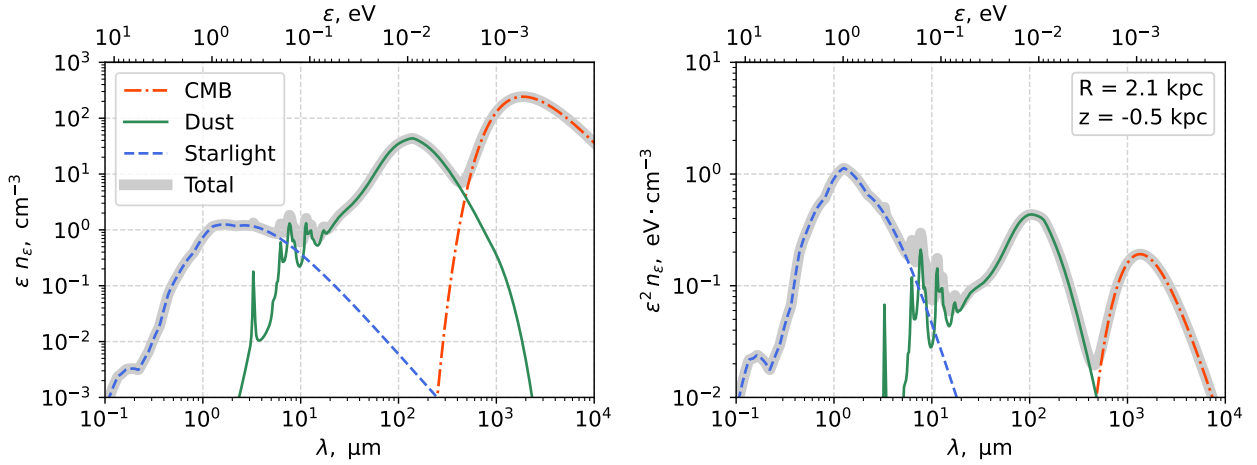


Figure 8: Background photon density (left) and energy density (right) in the vicinity of V4641 Sgr: CMB (red, dash-dotted), Dust (green, solid), Starlight (blue, dashed) and their sum (gray, bold).

Gas density

Several models for hydrogen distribution in the central part of the Galaxy predict local deficit of ionized (HII), atomic (HI) or molecular hydrogen (H_2) with densities $n_p = 0.006 \text{ cm}^{-3}$ [45] and $n_p = 0.03 \text{ cm}^{-3}$ [46] in comparison to average proton density in the surroundings of the Sun $n_\odot \sim 5 \text{ cm}^{-3}$.

Nevertheless, these galactic-average modes, designed to describe of the Galaxy as a whole, are insensitive to local features of a specific location in the Milky Way. Fortunately, in case of protons one can use 3D HI and CO maps to infer some information on density near the source, which will be done in section 4.

1.5. Extended radiation from the source: X-Ray to Gamma

In October 2024, HAWC collaboration reported detection of gamma-ray emission from V4641 region at 8.8σ for $E > 1$ TeV and at 5.2σ for $E > 100$ TeV (see [Figure 9 a,b](#)) [4]. From this observation one can see a 130 pc¹ elongated symmetric region in all energies (a), and a longer (200 pc) bright area at $E > 100$ TeV, which is slightly longer to the South of the source.

In the same month, LHAASO collaboration also issued a report on an extended source at 8.1σ for $E > 25$ TeV [5] ([Figure 9c](#)). Even with a large point-spread function (PSF) of this experiment at lower declinations (PSF $\sim 0.6^\circ$), the source cannot be considered point-like. From the TS map, we again infer the source elongation and North-South asymmetry.

H.E.S.S. collaboration also reported preliminary detection of the source for $E > 1$ TeV [6] ([Figure 9d](#)). At these lower energies, we clearly see a smaller region (110 pc) of complex shape and structure. The smallest PSF among the three high-energy gamma-ray detectors (~ 0.07 , [47, 48]) allows to speculate about resolving the width of the region, which in the provided TS map is several times larger than PSF.

These three observations cover the energy-range from 1 TeV up to 800 TeV, which makes the gamma-ray nebula around V4641 one of the brightest and energetic sources in the Galaxy. At lower energies, in the working diapasone of the Fermi telescope, the radiation was not detected, but the upper-limits were calculated [29, 30, 6].

All the results of observed extended radiation, layered one on top of the other, are shown in [Figure 9f](#). We make emphasis on three main features of the nebula:

- Length of the source, increasing with energy;
- Non-zero width of the filament: H.E.S.S. PSF is several times smaller than the detected orthogonal scale of the nebula;
- North-South asymmetry especially visible at $E > 100$ TeV in both HAWC and LHAASO.

The models we develop for the nebula are to explain all these features.

Additionally, in March 2025, the registration of extended emission in X-Ray from the central part of the region from analysis of XRISM data [9] ([Figure 9e](#)). The authors presented three different flux models, two of which are based on synchrotron emission of high-energy electrons, and the last one is connected to thermal emission from plasma at $T = 3.2 \pm 0.7$ keV.

The point corresponding to the preferred model (case (b) in Table 1 of [9]) is shown in [Figure 4](#) with a black solid cross; the flux with subtracted galactic X-ray emission background (GRXE) is also depicted there with a black dotted cross.

¹Here and further by the size of the nebula we mean its approximate projected length along its major axis for $d = 6.1$ kpc.

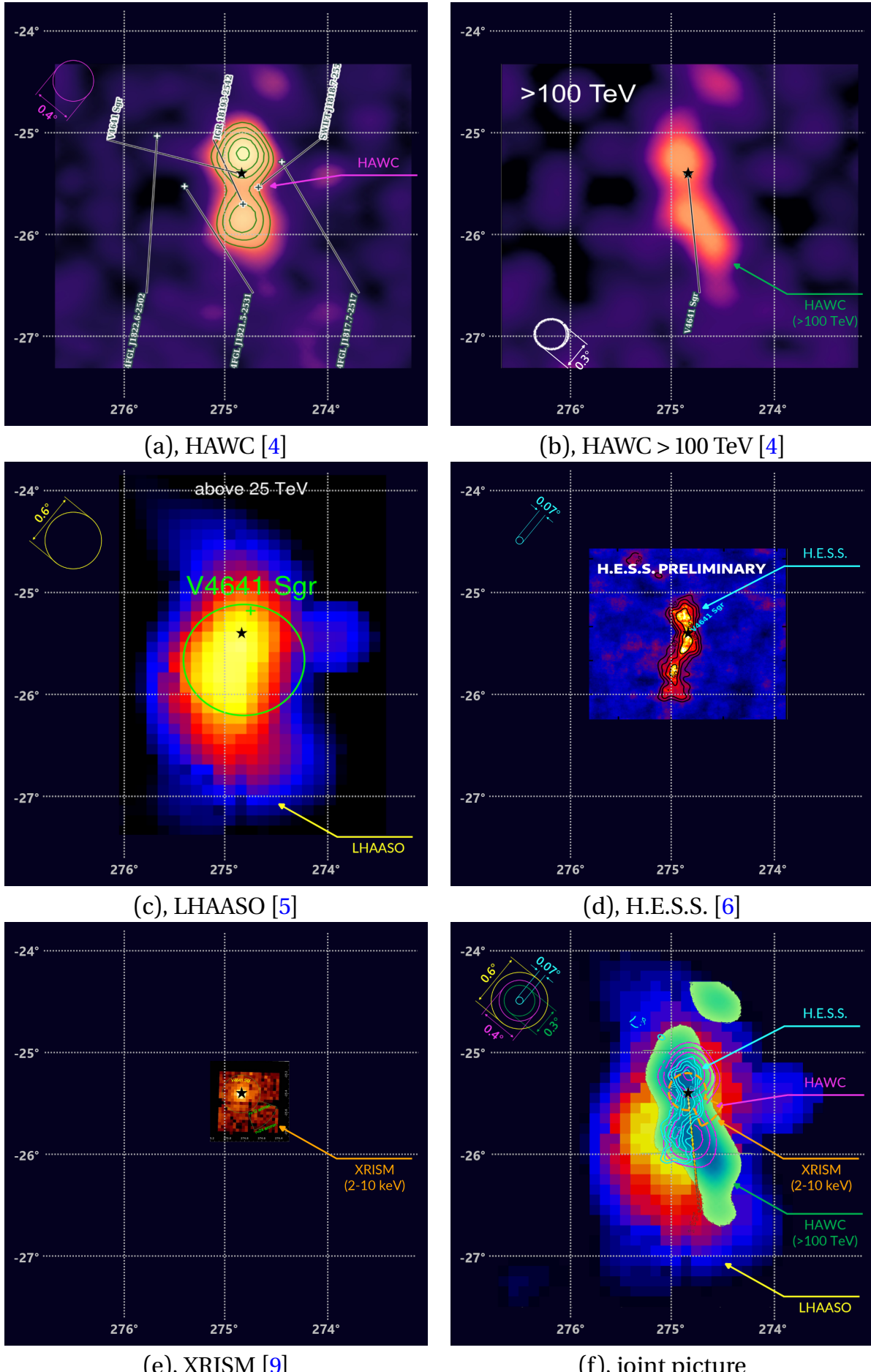


Figure 9: High-energy and extended X-Ray observations of the nebula around V4641 Sgr.

High-energy spectrum of the source

All three ultra-high-energy observations made by H.E.S.S., HAWC and LHAASO are accompanied by spectral measurements.

Gamma-ray measurements made on Earth differ from the intrinsic spectra due to UHE gamma-ray attenuation on background radiation field, described in subsection 1.4, via electron-positron pair-production.

$$\gamma_{\text{HE}} + \gamma_{\text{bg}} \rightarrow e^+ + e^- \quad (1.1)$$

The rate of this process is governed by Klein-Nishina cross-section, and is proportional to background density. Hence, main contributor to attenuation are CMB photons (of average energy 4 meV). As pair-production reaction (1.1) has a threshold $\epsilon_{\text{HE}}\epsilon_{\text{bg}} \geq 2m_e^2$, attenuation on CMB starts from $\sim 10^{14}$ eV, which can be seen from the Figure 10.

For technical reasons, the calculation was done with the use of a radiation model [49], different from the one, shown in Figure 8. These two models show a good coincidence in the infrared region, while experience a factor of 5 difference in optical domain, whose influence on galactic medium transparency is negligible.

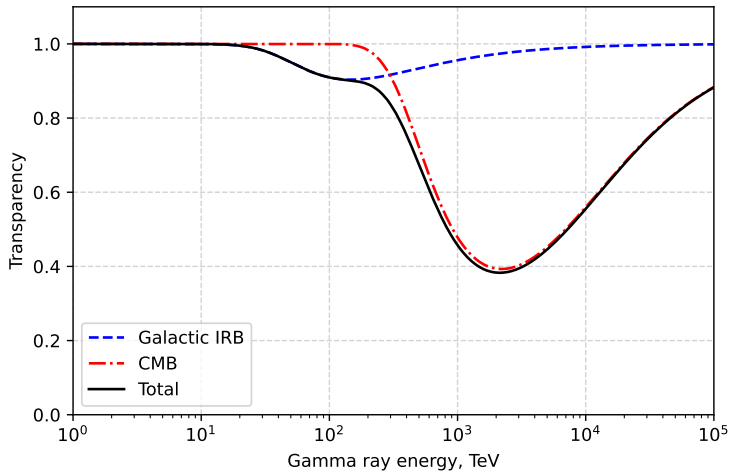


Figure 10: Galactic medium transparency (observed/intrinsic flux ratio) for V4641 at $d = 6.1$ kpc with dust radiation model from [45, 49].

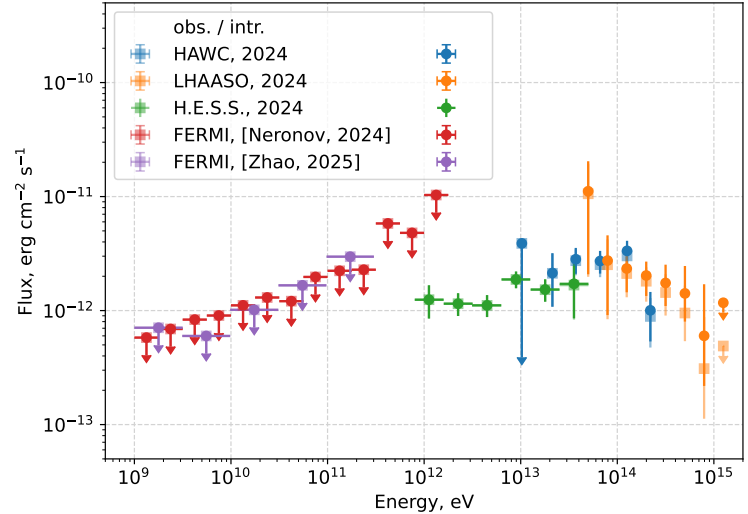


Figure 11: Observed (pale) and emitted (bright) gamma-ray spectra restored from pair-production attenuation.

2. Cosmic Ray Transport

High-energy gamma radiation in Galaxy is usually connected either to Inverse-Compton scattering of electrons on external radiation fields or to secondary photon production in hadronic interactions with interstellar medium. In this section we look through several possible scenarios for the observed UHE nebula to occur and evolve in the framework of Cosmic-Ray transport.

2.1. General remarks

Particle's trajectory in magnetic field is controlled by the Lorentz force

$$\frac{d}{dt}\gamma m\mathbf{v} = \frac{q}{c}[\mathbf{v} \times \mathbf{B}], \quad (2.1)$$

where m is the mass of the particle, \mathbf{v} is its velocity, $\gamma = (1 - v^2/c^2)^{-1/2} = E/mc^2$ is the corresponding gamma-factor, q is the charge, and $\mathbf{B} = \mathbf{B}_0 + \delta\mathbf{B}$ is total local magnetic field vector, that consists of a regular part \mathbf{B}_0 (aligned with z -axis) and a turbulent component $\delta\mathbf{B}$.

As we consider only electrons and protons, we set $|q| = e$.

A regular part can be characterized by two well-determined values: Larmor (gyration) frequency Ω_g and radius r_g :

$$\Omega_g = \frac{eB_0}{\gamma mc} = \frac{eB_0c}{E}, \quad r_g = \frac{p_\perp}{eB_0} = \frac{v_\perp}{\Omega_g}. \quad (2.2)$$

Maximal gyration radius of the particle corresponds to $\alpha = 90^\circ$:

$$r_g^{\max} = \frac{E}{eB_0} \simeq 1 \text{ pc} \left(\frac{E}{\text{PeV}} \right) \left(\frac{\mu\text{G}}{B_0} \right).$$

Hence, even for very-high-energy particles, the characteristic distances in the nebula significantly exceed their gyroradius. Therefore, in the following discussion, we can apply *the guiding center approximation* and consider particle motion averaged over the gyration period.

In a pure regular field, an UHE particle is spiralling along the field line with the velocity $v_{\parallel} = c \cos \alpha$, defined by the pitch angle $\alpha = \angle(\mathbf{v}, \mathbf{B}_0)$. This straight spiraling movement we refer to as *ballistic regime*. In this case, $\langle \Delta z \rangle = v_{\parallel} t$

The turbulent GMF component δB excites the particle's trajectory and alters its longitudinal momentum. This, in turn, either causes the particle to change direction (giving rise to the longitudinal diffusion), or shifts it to a different GMF line (resulting in the UHE-beam broadening and thus inducing transverse diffusion).

A complete transition from ballistic to *diffusive regime*, in which the particle no longer "remembers" its initial velocity, occurs when the average inclination angle exceeds 90° [50]. In comparison to the ballistic case, here $\langle \Delta z^2 \rangle \sim D_{\parallel} t$, where D_{\parallel} is parallel diffusion coefficient.

2.2. Ballistic regime

Consider a one-dimensional, non-collisional particle transport along the z -axis, with a source at $z = 0$ and a fixed particle velocity v . One can write two transport equations for particles moving to the right (n_+) and to the left (n_-):

$$\frac{\partial n_{\pm}}{\partial t} \pm v \frac{\partial n_{\pm}}{\partial z} = \frac{1}{2} q(z, t), \quad (2.3)$$

Each of these equations has a straightforward solution with a causal Green's function:

$$G_{\pm}(z, t) = \delta(vt \mp z). \quad (2.4)$$

It is natural to introduce the total particle density and flux as $n = n_+ + n_-$ and $j = j_+ + j_- = v(n_+ - n_-)$. By adding and subtracting the transport equations and changing variables accordingly, one arrives at a one-dimensional wave equation describing the dynamics of the total density:

$$\frac{\partial^2 n}{\partial t^2} - v^2 \frac{\partial^2 n}{\partial z^2} = \frac{\partial q}{\partial t}. \quad (2.5)$$

The corresponding Green's function is simply the half-sum of G_+ and G_- from (2.4):

$$G(z, t) = \frac{1}{2} [\delta(vt - z) + \delta(vt + z)]. \quad (2.6)$$

In this regime, as expected, the ejected particles simply spread out from the source at a constant speed.

Among the three nebular features discussed in subsection 1.5, the ballistic regime fails to explain both the increasing asymmetry of the source and its energy-dependent size. The latter is a well-known hallmark of diffusive cosmic-ray transport.

2.3. Diffusive regime

Anisotropic diffusion equation

In a turbulent magnetic field, after a sufficiently long time, the effects of magnetic mirroring and pitch-angle scattering cause particles to lose memory of their initial conditions [51]. In this regime, cosmic-ray transport is described by a three-dimensional anisotropic diffusion equation:

$$\partial_t n - \partial_i (D_{ij} \partial_j n) = q(\mathbf{r}, t), \quad (2.7)$$

where D_{ij} is the general diffusion tensor. Under the assumption of a constant regular magnetic field B_0 and an isotropic turbulent component δB , the diffusion tensor can be diagonalized, yielding a simplified form of the equation:

$$\partial_t n - D_{\perp} \left(\frac{\partial^2 n}{\partial x^2} + \frac{\partial^2 n}{\partial y^2} \right) - D_{\parallel} \frac{\partial^2 n}{\partial z^2} = q(\mathbf{r}, t). \quad (2.8)$$

In the form (2.8), the D_{ij} tensor reduces to $D = \text{diag}(D_\perp, D_\perp, D_{\parallel})$, where D_{\parallel} is the diffusion coefficient along the direction of the regular magnetic field, and D_\perp is the diffusion coefficient in the orthogonal directions.

In the following discussion, we focus on the ejection that began at $t = 0$, lasted until $t = T$, and is observed at times $t \geq T$.

$$n(\rho, t) = \frac{QT}{4\pi\hat{D}T\rho} \left[\text{erf}\left(\frac{\rho}{\sqrt{4\hat{D}(t-T)}}\right) - \text{erf}\left(\frac{\rho}{\sqrt{4\hat{D}t}}\right) \right]. \quad (2.9)$$

Effective diffusion coefficient here is defined as $\hat{D} = (D_{\parallel}D_{\perp}^2)^{1/3}$, and the anisotropic distance ρ is given by $\rho^2 = (x^2 + y^2) \left(\frac{D_{\parallel}}{D_{\perp}}\right)^{2/3} + z^2 \left(\frac{D_{\perp}}{D_{\parallel}}\right)^{2/3}$ (for derivation see [Appendix A](#)).

Diffusion coefficients

Diffusion coefficients in the Galactic medium effectively depend on the ratio of turbulent to regular magnetic field components, $\delta B/B_0$, and on the particle gyroradius, which scales as $r_g \propto E/B_0$ [50]. In the case $\delta B \ll B_0$, the statistical behavior of particles can be described within the framework of quasi-linear theory (QLT) [53]. As the turbulent component increases, analytical approaches break down, and numerical simulations must be used instead [54, 52, 55]. In such studies, the effective diffusion coefficients are defined as $D_{\parallel} = \frac{\Delta z^2}{\Delta t}$, $D_{\perp} = \frac{\Delta x^2}{\Delta t} = \frac{\Delta y^2}{\Delta t}$.

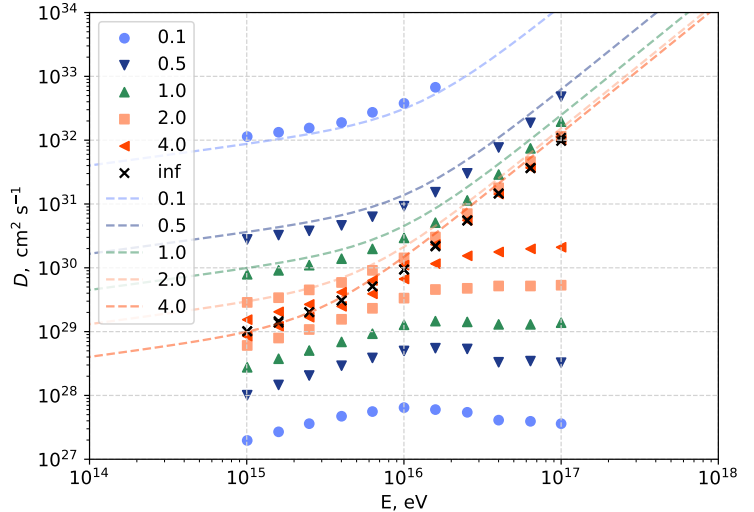


Figure 12: Diffusion coefficients (parallel on top and orthogonal at the bottom) for cosmic-rays in $1 \mu\text{G}$ magnetic field for $l_c = 20 \text{ pc}$ and Kolmogorov turbulence spectrum [52] and a QLT approximation for D_{\parallel}

As shown in [Figure 12](#), two diffusion regimes emerge: below 1 PeV, the diffusion coefficient scales as $D \propto E^{1/3}$, while above this energy, $D \propto E^2$. From (??) and (??), the characteristic diffusion length is given by $L_{\text{dif}} = \sqrt{4Dt}$, leading to $L_{\text{dif}} \propto E^{1/6}$ at low energies and $L_{\text{dif}} \propto E$ at high energies. This naturally explains the observed size-on-energy dependence of the nebula.

Nevertheless, the diffusive regime has a fundamental drawback at short times: since $L_{\text{dif}} \propto t^{1/2}$, the effective propagation velocity scales as $v \propto t^{-1/2}$, becoming formally infinite as $t \rightarrow 0$. To address this issue, we next discuss the transition from the ballistic to the diffusive regime.

H.E.S.S. profile fitting

From (2.9) one can see that emission shape effectively depends on two parameters only: $\sqrt{4D(t - T)}$ and $\sqrt{4Dt}$, as QT is total number of emitted particles. Using this, we conducted a simple χ^2 -based analysis to impose constraints on nebula's lifetime.

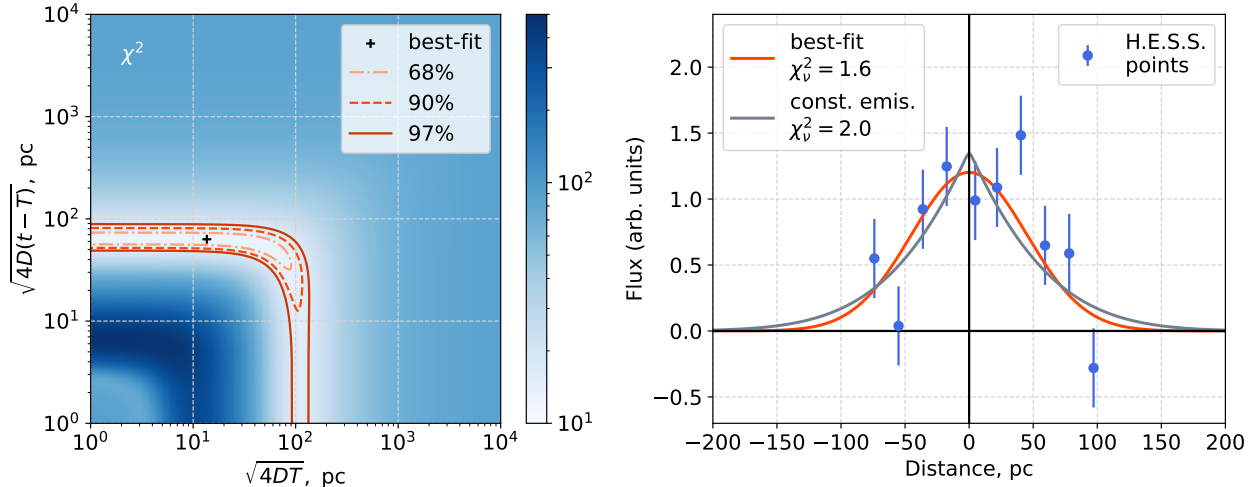


Figure 13: *Left:* χ^2 map for emission $\sqrt{4DT}$ and silent $\sqrt{4D(t - T)}$ timescales with several confidence levels: 68%, 90% and 97%. *Right:* the best-fit profile (11.8, 63.3) pc and a constant-emission profile (115.1, 1.0) pc.

Left panel of Figure 13 shows a χ^2 statistics map as a function of parameters of our interest with 68%, 90% and 97% upper contours. Based on this plot we can constrain the silent timescale parameter $\sqrt{4D(t - T)}$ to be > 12.6 pc (66 yr)² at 90%, and > 32.3 pc (433 yr) at 68% confidence levels, which means that *we prefer a flash-like profile to a continuous one*. Maximal value for the silent timescale is set to be 89.4 pc (3317 yr) at 97% confidence level, which corresponds to maximal flash-like emission time.

In the same way one can constrain $\sqrt{4DT}$, which does not have a lower limit, but has an upper one at the value of 105 pc (4576 yr), which corresponds to maximal continuous emission.

Here we note that these estimations are performed under *a strong assumption that the filament is orthogonal to the line-of-sight*. If we add a projection angle parameter θ , due to the fact that H.E.S.S. sees a narrow nebula, we can correct projected propagation time by $T_{\text{real}} = T/\cos \theta$.

2.4. Ballistic-Diffusive transition

Diffusive transport regime requires some time to set up. If in all-galaxy cosmic-ray transport investigation the settling time is usually not taken into consideration, on small-scales the transition from ballistic to diffusive regime can play a crucial role in particle dynamics.

²The values in brackets correspond to standard diffusion coefficient $D = 10^{30} \text{ cm}^2 \text{ s}^{-1}$ in a $1 \mu\text{G}$ field at 6 TeV, average H.E.S.S. detection energy

If turbulent field is smaller than the regular component ($\delta B \ll B_0$), one can apply QLT to calculate the *diffusion length* — a characteristic scale on which a particle deviates significantly from its initial trajectory (see eq. (3.43) in [53]).

$$\lambda_{\parallel} = \frac{3L_0}{16\pi C(s/2)} \left(\frac{B_0}{\delta B} \right)^2 \left[\frac{4}{(2-s)(4-s)} \left(\frac{r_g}{L_0} \right)^{2-s} + \left(\frac{r_g}{L_0} \right)^2 \right], \quad (2.10)$$

where L_0 is characteristic turbulence scale, s is turbulence power spectrum index ($s = 5/3$ for Kolmogorov, $s = 5/2$ for Kraichan), $C(s/2)$ is a numerical factor close to 0.1.

A simple derivation of the power-laws in (2.10) is performed in [Appendix B](#)

Generally speaking, unless $l < \lambda_{\parallel}$ (or $t < \tau_{\parallel}$), particle's transport can be considered as free propagation, after that, the particle behavior becomes closer and closer to diffusion.

Telegrapher's equation for Ballistic-Diffusive transition

The proper description of the ballistic-diffusion transition in galactic environment is a complicated topic for numerical simulations of high-energy particles propagating in plasma. For the moment, there is no general consensus on description of this process, despite the fact that several attempts were made in this direction [56, 57]

In order to sketch the transition, we use the one-dimensional telegrapher's equation, as proposed in [58, 59, 60]:

$$\frac{\partial^2 n}{\partial t^2} + \frac{1}{\tau} \frac{\partial n}{\partial t} - v^2 \frac{\partial^2 n}{\partial z^2} = \frac{\partial q}{\partial t} + \frac{q}{\tau}, \quad (2.11)$$

which reduces to (2.5) for $t \ll \tau$, or to 1D-version of (2.8) for $t \gg \tau$ with $D_{\parallel} = v^2 \tau$.

In order to account for diffusion in orthogonal direction, we multiply the one-dimensional solution by diffusive part that is given by the following equation

$$\frac{\partial n_{\perp}}{\partial t} - D_{\perp} \left(\frac{\partial^2 n_{\perp}}{\partial x^2} + \frac{\partial^2 n_{\perp}}{\partial y^2} \right) = q_{\perp}(r_{\perp}, t). \quad (2.12)$$

A toy-model to derive (2.11), form of its Green's function with ballistic and diffusive limits can be found in [Appendix C](#).

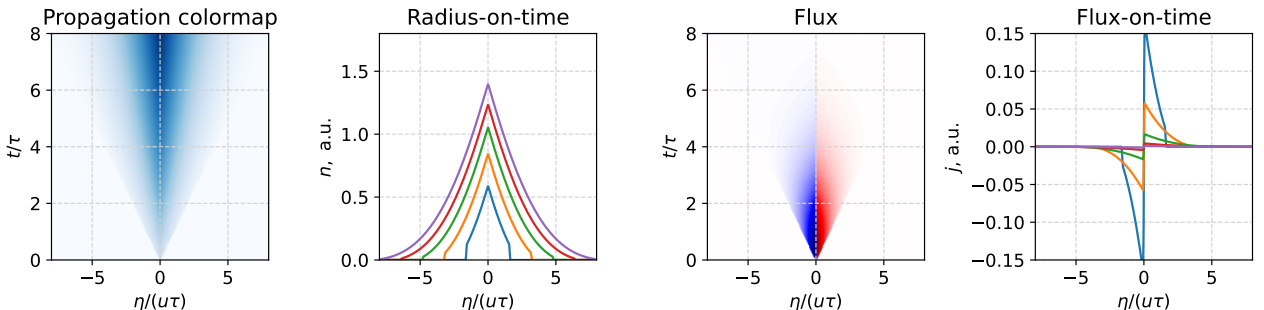


Figure 14: Telegrapher's equation profile (left) and fluxes (right) as a function of time (in diffusion timescales τ) and coordinates (in $v\tau$).

3. Leptonic model

The first thing an apprentice in astrophysics must consider is trying to explain all the peculiarities of the chosen high-energy gamma-ray source without resorting to hadronic processes. This section is dedicated to the construction of a self-consistent leptonic model of a high-energy nebula detected in the vicinity of the binary V4641.

3.1. Interactions and Timescales

Electrons have a wide range of ways to interact with their surroundings: they cool by emitting synchrotron radiation in external magnetic fields, scatter off low-energy background photons like those from the CMB or ISRF (see subsection 1.4), and diffuse as they bounce off the turbulent components of magnetic fields.

Inverse Compton scattering

In this work, as is common in astrophysics, we refer to the elastic upscattering of a low-energy background photon by an ultra-high-energy electron as *Inverse Compton scattering* (IC). The background radiation is assumed to be isotropic, which, as shown in [61], allows for the derivation of analytical expressions for the high-energy photon spectrum produced by ultrarelativistic electrons.

In Figure 15, we show the spectra of photons scattered by monoenergetic high-energy electrons interacting with an isotropic CMB background. For relatively low-energy electrons, one can apply the so-called *Thomson limit*. In this regime, the energy of the incoming photon in the electron rest frame is negligible compared to the electron's mass: $\epsilon' \ll m_e c^2$.

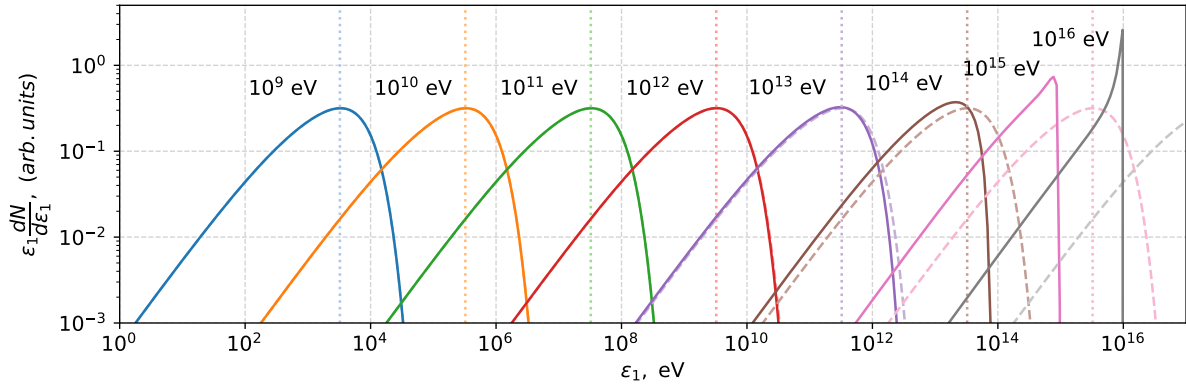


Figure 15: Normalized photon spectra from monoenergetic electrons (from 10^9 to 10^{16} eV) scattering on CMB. Solid lines correspond to a calculation that uses full Klein-Nishina formula; dashed lines are obtained in Thomson limit. Vertical dotted lines correspond to average photon energy in Thomson limit. The presented spectra were calculated with the formulae given in [61] and compared to [62].

There is a simple expression for an average upscattered photon energy in the Thomson limit: $\langle \epsilon_1 \rangle = \frac{4}{3} \gamma^2 \langle \epsilon \rangle$. For the CMB, $\langle \epsilon \rangle = \frac{3\zeta(4)}{\zeta(3)} k_B T_{\text{CMB}} \approx 2.70 k_B T_{\text{CMB}} = 6 \cdot 10^{-4}$ eV. Moreover, electron energy-loss rate expression turns out to be rather simple:

$$-\dot{E}_{\text{IC,Th}} = \frac{4}{3} \sigma_T c \gamma^2 U_{\text{rad}}. \quad (3.1)$$

At electron energies above $E > (m_e c^2)^2 / 2\epsilon$ (10^{14} eV for CMB, 10^{12} eV for dust thermal photons and 10^{11} eV for starlight), the scattering pattern changes, exhibiting a peak near the energy of the scattered electron. This indicates that at high energies — in the *Klein–Nishina regime* — Inverse Compton scattering becomes an efficient energy loss mechanism, and upscattered photons take away almost all energy of the electron. Energy losses in general case can be computed from

$$-\dot{E}_{\text{IC}} = \int (\epsilon_1 - \epsilon) \frac{dN}{dt d\epsilon_1} d\epsilon_1. \quad (3.2)$$

Synchrotron Radiation

Broad-range photon emission by electrons spiraling along magnetic field lines is called *synchrotron radiation*. According to Weizsäker–Williams approach, this process can be treated as Compton scattering of electrons on virtual photons of the magnetic field [61].

The *received* spectral power of synchrotron radiation from a single electron with energy E in a magnetic field B at a pitch angle α is given by

$$P_{\text{syn}}(\epsilon, E, \alpha) = \frac{\sqrt{3}e^3 B}{mc^2 \sin \alpha} F(\epsilon/\epsilon_c), \quad \epsilon_c = \frac{3eBcE^2 \sin \alpha}{4\pi(mc^2)^3} \approx 66.5 \text{ keV} \sin \alpha \left(\frac{E}{\text{PeV}} \right)^2 \left(\frac{B}{\mu\text{G}} \right), \quad (3.3)$$

where $F(x) = x \int_x^\infty d\xi K_{5/3}(\xi)$ is called *the first synchrotron function*. Its well-known asymptotic behavior allows for the construction of a simple and accurate fit [63], which we use in subsequent calculations.

Electron energy losses for a pitch-angle α are given by integration of *emitted* synchrotron radiation power

$$-\dot{E}_{\text{syn}} = \frac{2r_0^2}{3c} \gamma^2 B^2 v^2 \sin^2 \alpha, \quad (3.4)$$

which in case of an isotropic distribution is identical to (3.1) with $U_{\text{rad}} = U_B = B^2 / 8\pi$.

A comprehensive discussion on IC and Synchrotron radiation calculations can be found in Appendix E.

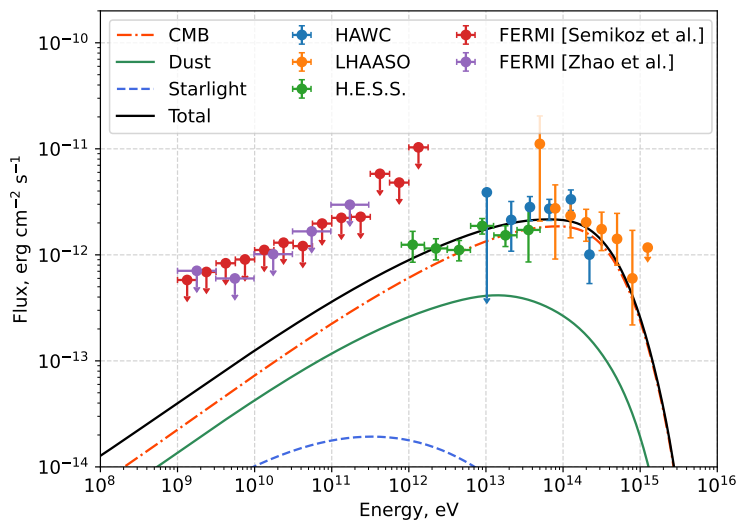


Figure 16: Inverse Compton radiation from electron spectrum with $\gamma = 2$, $E_{\text{cut}} = 630$ TeV, $E_{\text{tot}} = 5 \cdot 10^{47}$ erg from each component of the background radiation: starlight (blue, dashed), dust (green, solid), CMB (red, dash-dotted), and total (black, solid).

Bremsstrahlung

Radiation emitted by an electron when it is deflected by another charged particle is referred to as *Bremsstrahlung* or *braking radiation*. From the perspective of the Weizsäcker–Williams technique, Bremsstrahlung can be treated as Compton scattering of virtual photons from the Coulomb field of the scattering center by the incoming electron [61].

Although energetically comparable to inverse Compton (IC) photons, the flux from Bremsstrahlung processes in cold, gas-poor environments ($n \sim 1 \text{ cm}^{-3}$) is usually much lower. We consider the amount of Bremsstrahlung photons negligible and do not take it into account in the present work.

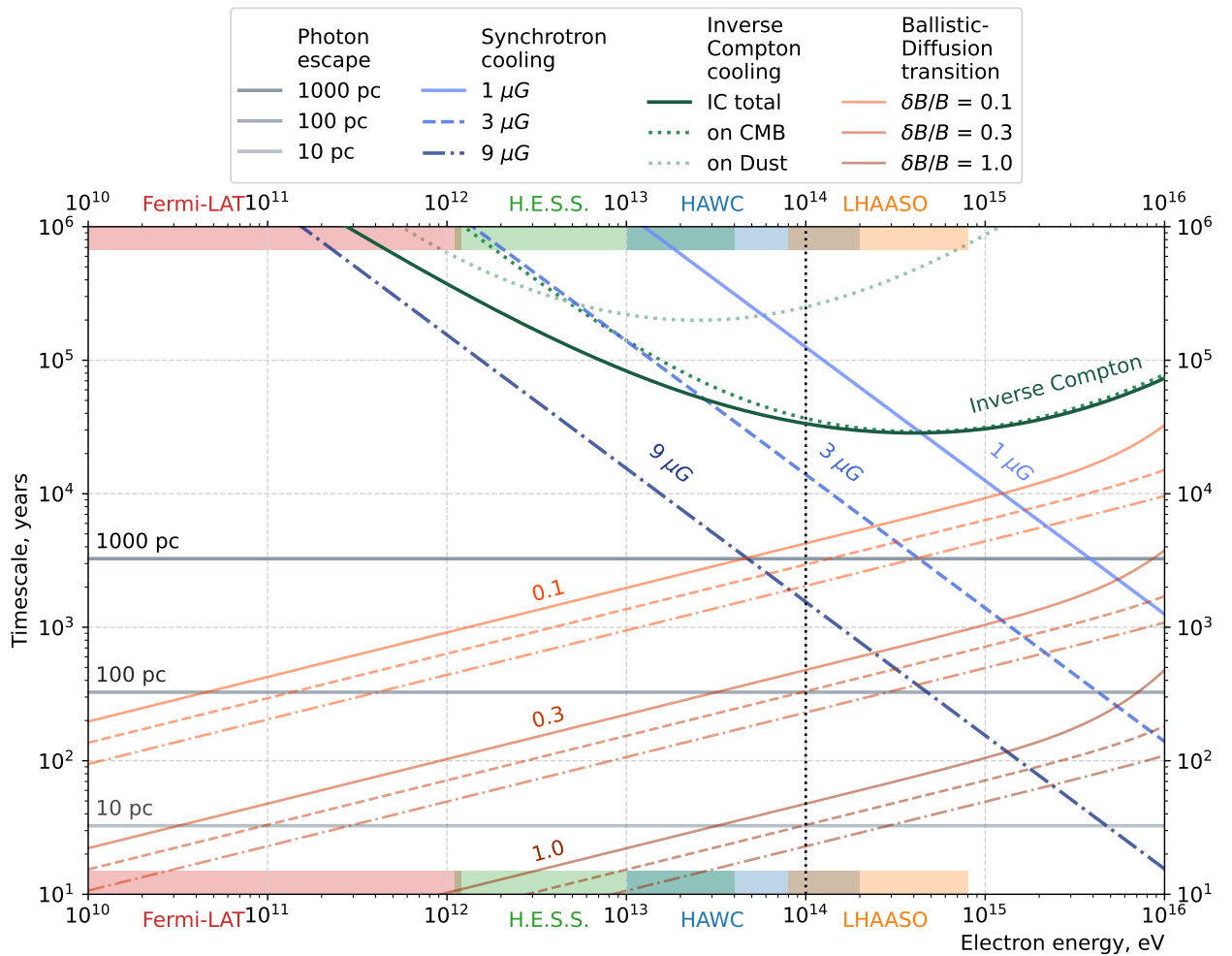


Figure 17: *Electron characteristic timescales*.

Gray: photon crossing times for path lengths of 10, 100, 1000 pc.

Shades of blue: synchrotron cooling timescales for magnetic field strengths of 1 μG (solid), 3 μG (dashed), and 9 μG (dash-dotted).

Shades of red: ballistic-diffusion transition timescales for different turbulent/regular field ratios. Solid lines correspond to magnetic field of 1 μG , dashed ones to 3 μG , and dash-dotted to 9 μG .

Corresponding timescales

Each of the processes, mentioned above, features a characteristic timescale, which are summarized in [Figure 17](#) for the energy-range of our interest.

- Photon crossing time: $t_{\text{phot}} = L/c$.
- Synchrotron cooling time: $t_{\text{syn}}(E, B) = E/\langle P_{\text{syn}}(E, B) \rangle$.
- Inverse Compton cooling time: $t_{\text{IC}}(E) = E/\langle P_{\text{IC}} \rangle$.
- Ballistic-Diffusion transition: $t_{\text{tr}}(E, B) = 3D_{\parallel}(E, B)/c$.

There are several parameters of the nebula which can be adjusted. They are

- Total magnetic field value $B = \sqrt{B_0^2 + \delta B^2}$, which defines synchrotron losses and affects diffusion coefficient values.
- Turbulent/Regular magnetic field ratio $\eta = \delta B/B_0$, which strongly affects ballistic-diffusion transition times and correspondingly, diffusion coefficients;
- Emission type: flash-like or constant ejection, which affects particle distribution profile and available electron energies in the nebula;
- Flare age or duration of electron emission T , which influences the shape of the nebula.

3.2. Single Flare Scenario

The most straightforward idea would be a description of the nebula with a population of electrons from a single flash, which occurred T years ago. For all its simplicity, there are several significant constraints for this scenario.

Gamma-ray spectrum, reported by HAWC, LHAASO, and H.E.S.S. collaborations with flux upper-limits from FERMI, with the known local radiation background, allows for an approximate calculation of the total number of electrons in the nebula. This, in turn, leads to an estimation of magnetic field in the nebula, required to obtain the X-Ray radiation level, measured by XRISM. In order for obtain sufficient synchrotron radiation level, magnetic field has to be at least $2 \mu\text{G}$. This means, that at higher energies and timescales $> 10^3$ yr, synchrotron losses for the population of electrons would play an important role.

The highest-energy gamma-ray photon from V4641 Sgr was reported by LHAASO Collaboration at 800 TeV. Accounting for synchrotron losses only (without IC losses), one can estimate maximum period of time during which high-energy photons will be present. From analytical solution of transport equation for cooling electrons (see [Appendix D](#))

$$C_{\text{syn}}EB^2t < 1, \text{ with } C_{\text{syn}} = \frac{\sigma_T}{6\pi m^2 c^2} \approx 7.7 \cdot 10^{-5} \mu\text{G}^{-2} \text{yr}^{-1} \text{PeV}^{-1}, \quad (3.5)$$

from where we obtain $\left(\frac{B}{\mu\text{G}}\right)^2 \left(\frac{t}{\text{yr}}\right) < 1.3 \cdot 10^4 \left(\frac{\text{PeV}}{E_{\text{max}}}\right)$. Thus, $B^2t < 16 \mu\text{G}^2 \text{kyr}$.

As XRISM measured X-Ray flux in a part of the area, total synchrotron from all the electrons in the nebula has to be rescaled. We assume here two electron distributions in the volume of the nebula, where $L \propto E^{1/3}$: a homogeneous electron distribution (showed in green with [Figure 18](#)), and a single-flash diffusion (gaussian) distribution (in red in the same figure).

In order to fit measured XRISM emission, we made a Monte-Carlo Markov Chain (MCMC) simulation of initial electron distribution with the following spectrum

$$\frac{dN}{dE} = \left. \frac{dN}{dE_0} \right|_{E_0} \cdot \exp \left\{ \eta - \gamma \ln \left(\frac{E}{E_0} \right) - \frac{E}{10^{k_2} E_0} \right\} \mathbf{1}(E > 10^{k_1} E_0), \quad (3.6)$$

where η , γ , k_1 , k_2 are four dimensionless parameters; $E_0 = 10^{12}$ eV, $dN/dE_0 = 10^{34}$ eV $^{-1}$. Another parameter for Markov Chain sampling is emission time.

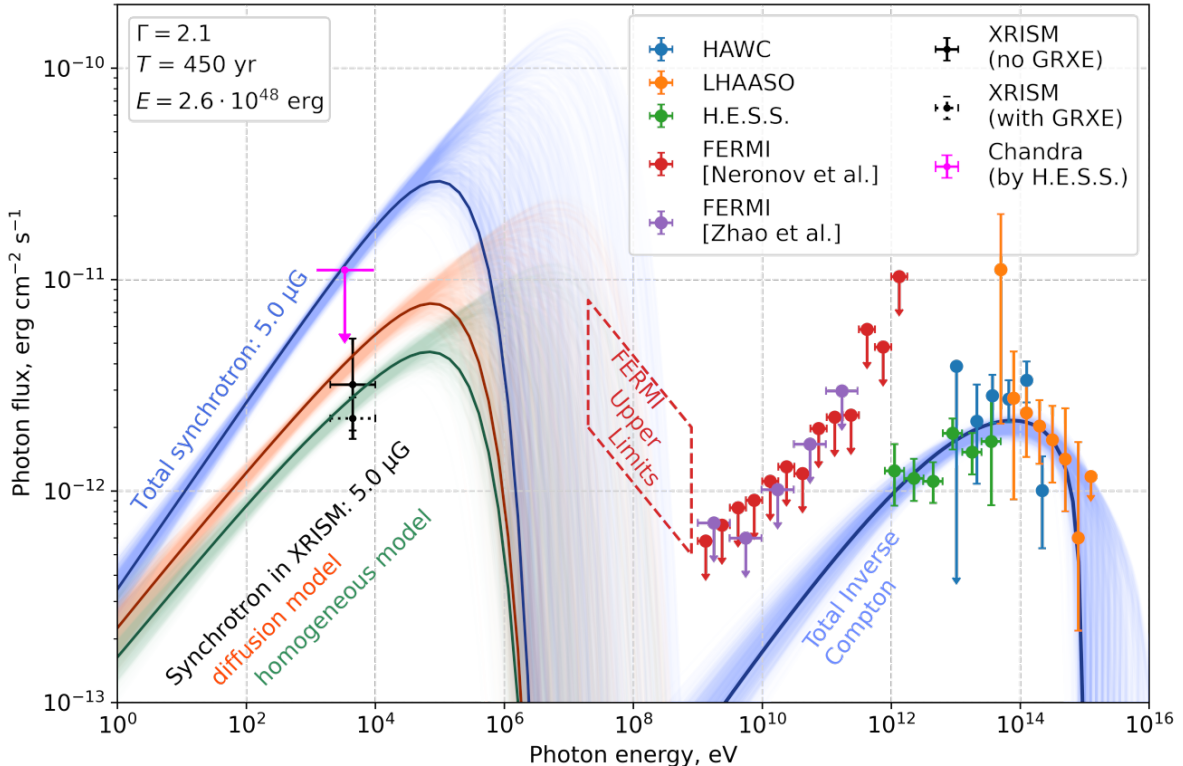


Figure 18: Total Inverse Compton (right, blue) and Synchrotron (left, blue) radiation peaks obtained via the MCMC simulation of the spectral evolution under the single-flare assumption.

After walking through magnetic fields from 1 to $10 \mu\text{G}$, optimal value turned out to be $5 \mu\text{G}$, which constrains lifetime to $T < 625 \text{ yr}$.

A three-parameter MCMC sampling with fixed $k_1 = -3$, $k_2 = 5$, shows that in order to maintain the flux measured by LHAASO, $T < 520 \text{ yr}$ (see Figure 19). Corresponding electron energy $E = 2.6 \cdot 10^{48} \text{ erg}$, which requires 100 yr of radiation with $L = L_{\text{Ed}}$, which does not correlate with current low activity of the binary.

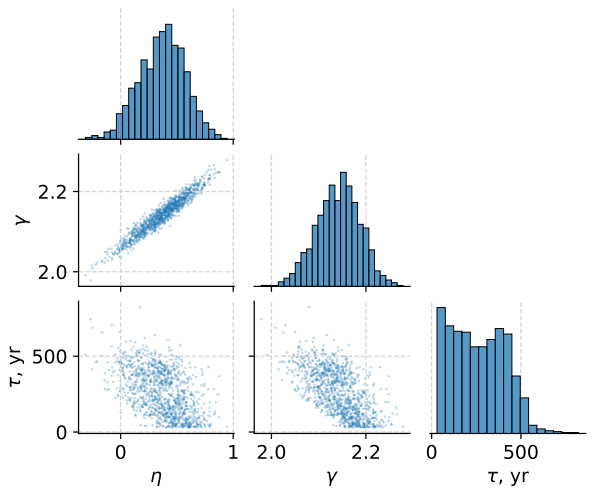


Figure 19: MCMC samples for η , γ , and τ .

This short lifetime is not consistent neither with diffusive, nor with ballistic scenario: even a straightforward propagation without spiraling in 500 yr does not allow to reach $L > 160$ kpc. *Thus, we disfavor a single flash scenario.*

3.3. Constant Emission Diffusive Scenario

Another reasonable assumption to make is that electrons are emitted constantly at low rate, or in regular flares of 1999 kind. These two assumptions can be considered equivalent if the time between flares is significantly smaller than the total time of electron accumulation in the nebula.

This assumption partially alleviates the main single-flash model constraint connected to keeping 800 TeV electrons in the nebula. Nevertheless, in order to maintain required amount of high-energy electrons, the ejected spectrum is to be steeper than in case of a single flare.

Constant emission profile is peaked at the source, thus the XRISM rescaling looks different. A conservative assumption would be that all the synchrotron radiation is inside the XRISM measuring zone. Taking into account both synchrotron and Inverse Compton cooling of electrons, we conducted a four-parameter MCMC study for this scenario (k_1 was again fixed to be -3) for magnetic fields from 1 to $10 \mu\text{G}$. In this case, magnetic field, as shown in Figure 20, has to be at least $2 \mu\text{G}$.

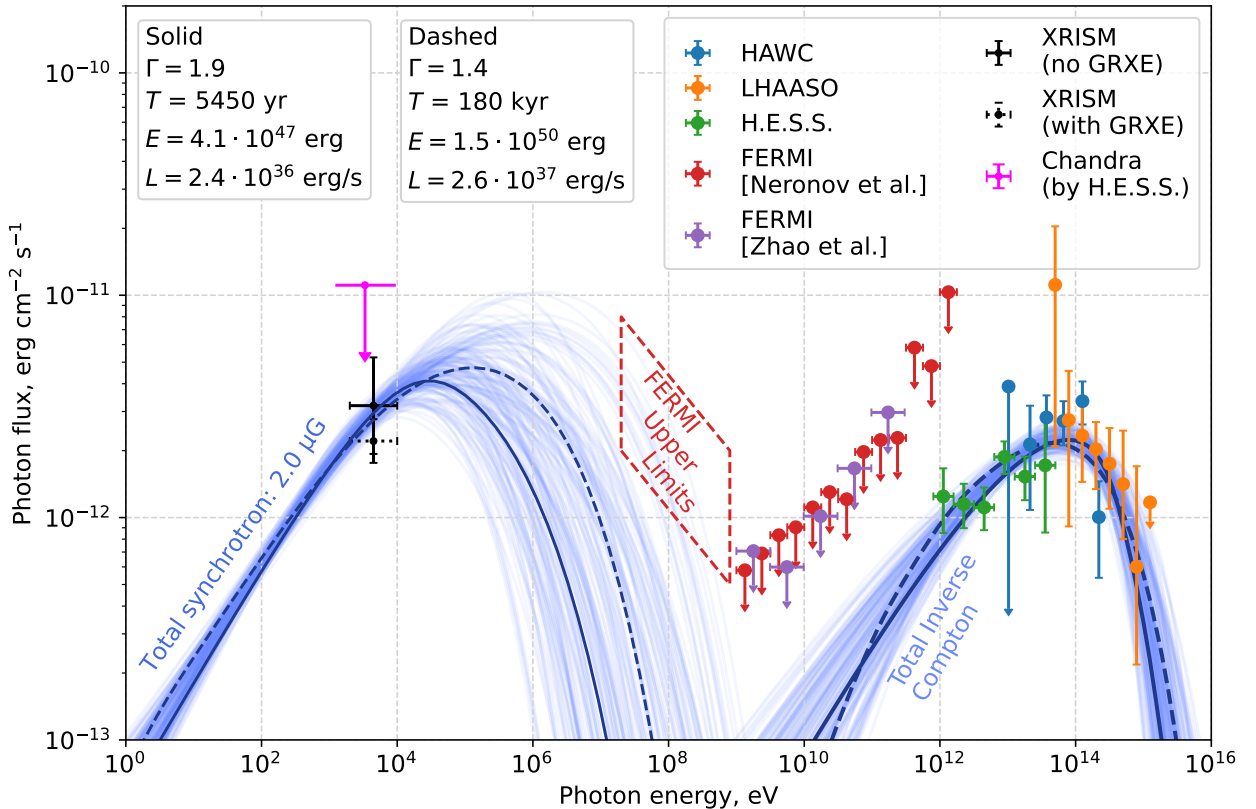


Figure 20: Total Inverse Compton (right, blue) and Synchrotron (left, blue) radiation peaks obtained via the MCMC simulation of the spectral evolution under the assumption of continuous electron emission.

In contrast to single ejection scenario, where the position of synchrotron peak is controlled by the age of the flare, here it is defined by maximum electron energy ejected from the source, which is constrained from below by LHAASO most energetic photons at 800 TeV.

[Figure 21](#) shows results of MCMC sampling for η , γ , k_2 , T for $B = 2 \mu\text{G}$. Here one can clearly see two data populations: a dominant one, which corresponds to $T < 10 \text{ kyr}$, and another one with much longer timescales. The second population corresponds to steady-state electron emission.

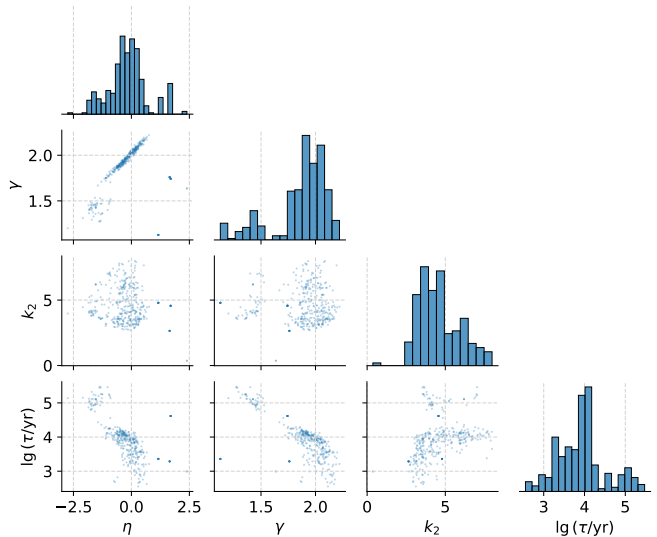


Figure 21: Sampling parameters of a continuous model.

Steady-state emission exclusion

In [Figure 20](#), we show all sampling results and two representative spectra from each population with their parameters stated in the upper-left corner of the image. We note that steady-state emission spectrum requires approximately order-of-magnitude higher luminosity which is $\sim 0.05L_{\text{Ed}}$. In other words, the steady-state case requires from the source to radiate for several weeks every year with Eddington luminosity, which is inconsistent with 60-year long observation of the binary.

Thus, steady-state electron emission is considered disfavored.

Continuous electron emission and propagation along the bent line

Energetically, the $\sim 5 \text{ kyr}$ continuous emission seems reasonable: when total emitted energy is of the order of $5 \cdot 10^{47} \text{ erg}$, average luminosity is $\sim 4 \cdot 10^{36} \text{ erg/s}$, which is only 1% of Eddington luminosity and probably can be achieved during minor flares, which the binary experiences approximately once per year.

To address the asymmetry feature of the nebula, one can bend the magnetic field lines, thereby shortening one of its edges, observed in a 2D projection. To achieve the desired result, we chose a constant magnetic field bending radius R_B and an axis around which the field line is bent. Geometric calculations show that $R_B \sim L_{\text{dif}}$ at lifetimes exceeding 15,000 years. The corresponding images, projected onto the rotation plane, the observed plane, and the y -axis, are shown in [Figure 22](#).

Therefore, we conclude that the continuous electron emission model successfully explains the observed spectrum in both the X-ray and gamma-ray domains. The energy-dependent length and width of the emission are attributed to diffusive propagation effects, while the nebular asymmetry can be accounted for by the bending of magnetic field lines.

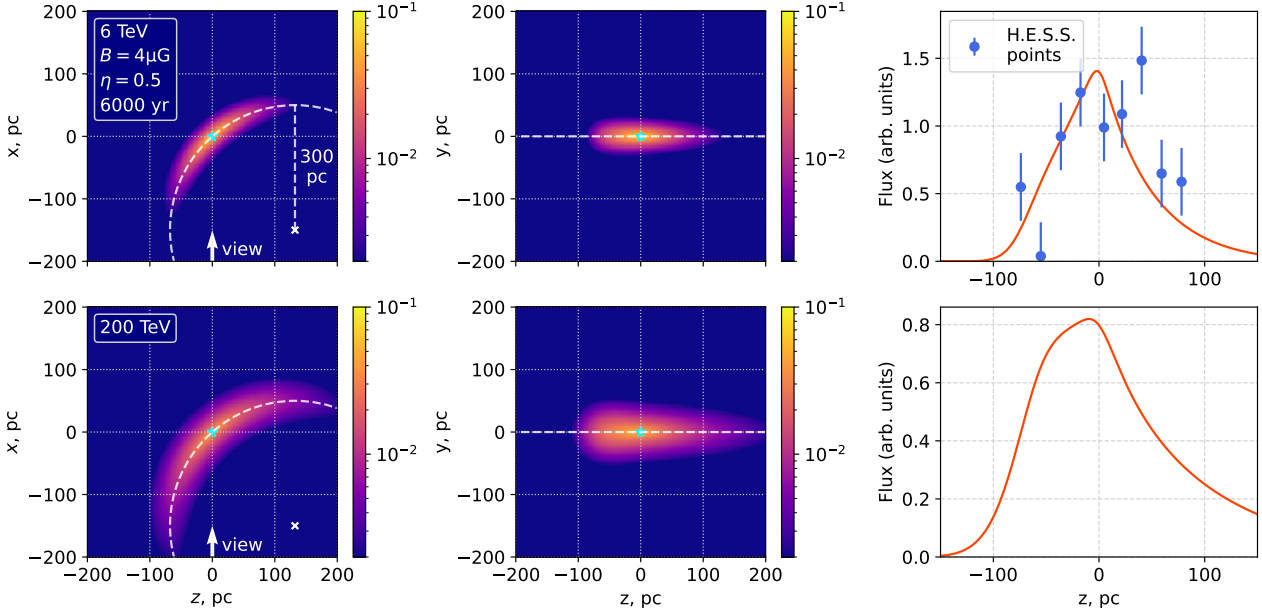


Figure 22: Diffusion profiles of a 6 kyr continuous emission in a curved regular magnetic field of $4 \mu\text{G}$ with curvature of $R = 300 \text{ pc}$ at 6 TeV (upper row) and 200 TeV.

3.4. Constant Emission Ballistic Transition Scenario

Magnetic field line bending is a commonly proposed explanation for the observed asymmetry of the gamma-ray nebula. However, this interpretation implies comparable fluxes from both the left (Northern) and right (Southern) regions of the nebula. While this condition is consistent with observations at lower energies, as reported by H.E.S.S. and HAWC, it becomes questionable at higher energies, particularly for HAWC observations above $E > 100 \text{ TeV}$ and in LHAASO data.

We propose an alternative explanation for the energy-dependent asymmetry of the source, which becomes more pronounced at higher energies. As shown in Figure 17, it is possible to identify a magnetic field strength for which the transition from ballistic to diffusive transport occurs on timescales of order 10^3 – 10^4 yr. At the energies of interest, and for magnetic fields $B \gtrsim 1 \mu\text{G}$, the diffusion coefficient follows the scaling $D \propto E^{1/3}$. As a result, the diffusion timescales at lower and higher energies can differ by a factor of 10. Thus, while particle transport in the H.E.S.S. energy range may already be dominated by diffusion, particles with energies above 100 TeV may still reside in the transition regime between ballistic and diffusive propagation.

Thus, if the magnetic field lines are inclined with respect to the plane orthogonal to the line of sight, the emission from diffusing particles will appear symmetric, as their transport becomes effectively isotropic over large timescales. However, for particles still in the free-streaming regime, the emission may exhibit anisotropy due to the preferred directions of synchrotron radiation and inverse Compton scattering, both of which are correlated with the direction of the electrons’ motion. Consequently, particles propagating forward — along the direction of the field inclination — will appear brighter than those moving in the opposite direction.

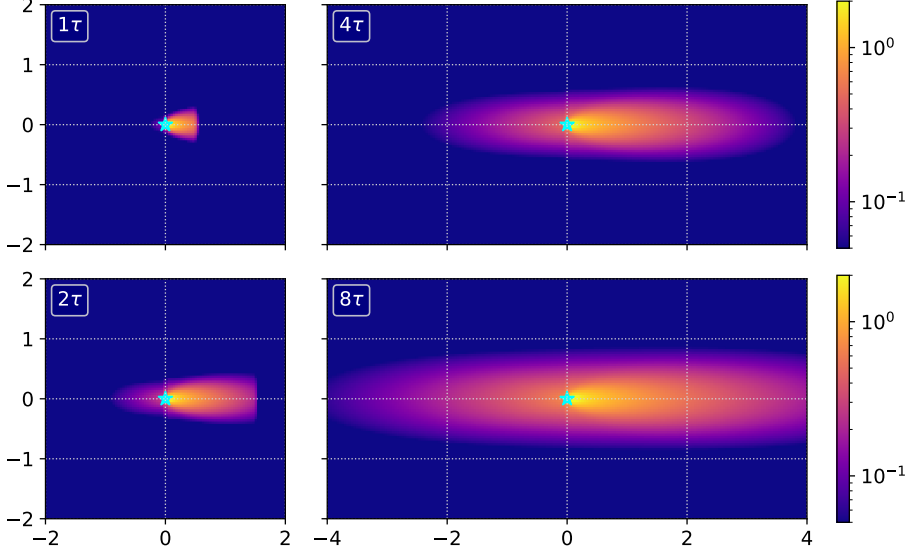


Figure 23: Ballistic-diffusion transition profiles from telegrapher’s equations at time units of diffusion times τ and in xz grid in $v\tau$ units.

In other words, if we introduce variables n_+ and n_- for the particles moving towards and from the observer respectively, such as $n = n_+ + n_-$ and $j = v(n_+ - n_-)$, the part responsible for radiation would be n_+ .

With the use of the toy model propagation with a simple collision term described in [Appendix C](#), we extracted n_+ from the equation and plotted [Figure 23](#), where one can see n_+ for various time moments. Here we note that constant particles supply makes the region close to the source always asymmetric. From visual comparison, $T = 4\tau$ for $E > 100$ TeV looks close to HAWC and LHAASO results.

As mentioned previously, the continuous electron emission model provides a satisfactory fit to the observed spectrum. Unlike the magnetic field line bending model, which faces difficulties reconciling the roughly equal North–South fluxes, the ballistic-diffusive model naturally predicts different flux levels at the nebula’s edges. However, this model requires the magnetic field lines to be oriented toward us at the southern edge of the filament.

Summary

In this section, we have constructed a leptonic model of the source, assuming continuous injection of high-energy electrons. These particles spiral along the regular magnetic field lines and diffuse due to the turbulent component. The minimal magnetic field strength required to account for the synchrotron emission observed by XRISM is estimated to be at least $2 \mu\text{G}$.

We propose two possible explanations for the observed North–South asymmetry of the source. The first relies on the bending of the regular magnetic field lines, which implies equal total fluxes from both ends of the nebula and requires the Northern side to be intrinsically brighter. The second explanation involves a transition from ballistic to diffusive transport at higher energies. This scenario requires fine-tuning of the emission lifetime and diffusion coefficient and leads to an unavoidable central asymmetry due to the directionality of particle propagation during the transition phase.

4. Hadronic Mechanism

As microquasars are considered to be the sources for galactic cosmic rays, the question of constructing a protonic model is of large importance to confirm or refute this assumption. In this section we construct a protonic model for the V4641 nebula and discuss its properties.

4.1. Interactions and Timescales

In contrast to electrons, electromagnetic interactions such as Inverse Compton scattering or synchrotron radiation are largely negligible for protons, as the corresponding cross-sections scale inversely with the particle mass. In hadronic models, the primary source of high-energy photons is the decay of neutral pions produced via inelastic proton-proton

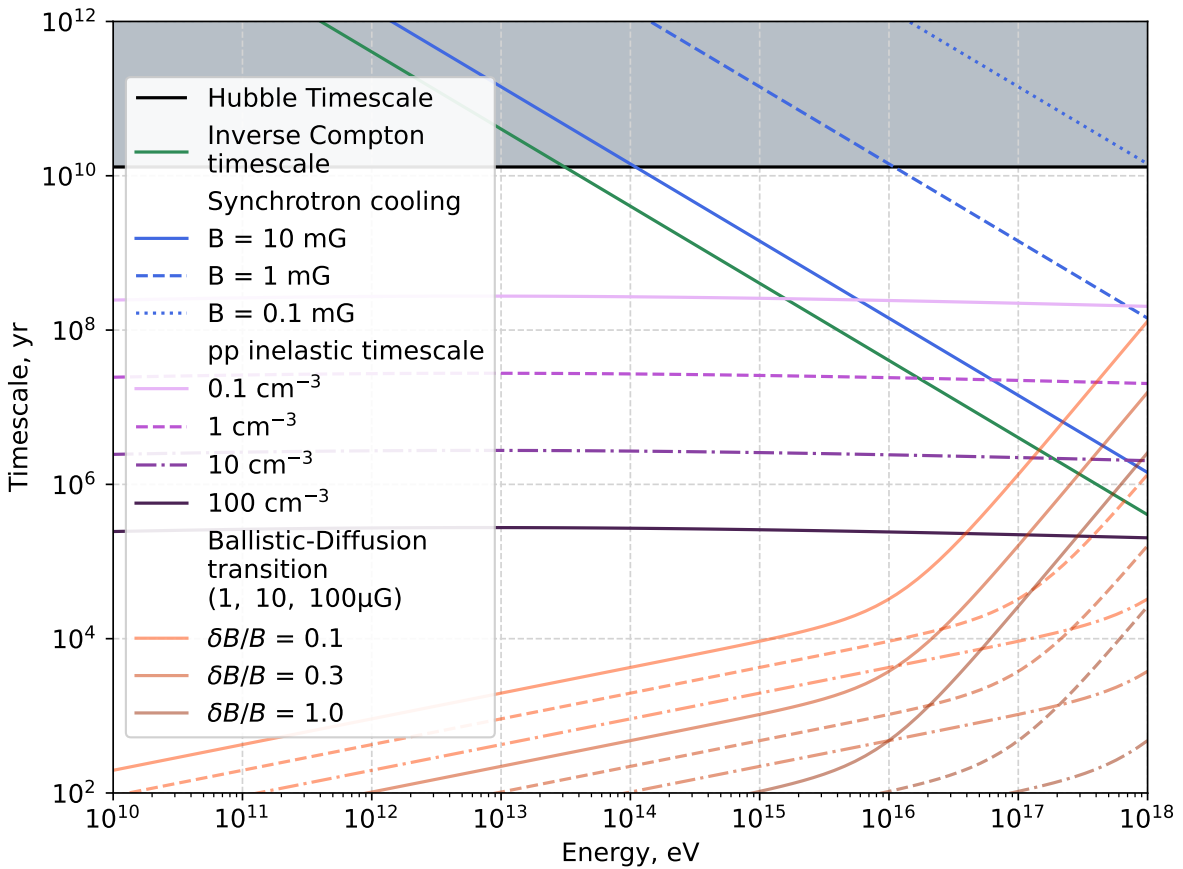


Figure 24: *Proton characteristic timescales.*

Black: Hubble timescale

Shades of blue: synchrotron cooling timescales for magnetic field strengths of 10 mG (solid), 1 mG (dashed), and 100 μ G (dotted).

Shades of red: ballistic-diffusion transition timescales for different turbulent/regular field ratios. Solid lines correspond to magnetic field of 1 μ G, dashed ones to 10 μ G, and dash-dotted to 100 μ G.

Green: Inverse-Compton scattering on background photons (Thomson limit).

Shades of violet: mean free path time for proton inelastic scattering on cold background protons for densities 0.1 cm^{-3} (bright, solid), 1 cm^{-3} (medium violet, dashed), 10 cm^{-3} (violet, dash-dotted), and 100 cm^{-3} (dark violet, solid).

collisions: $pp \rightarrow \pi^0 \rightarrow \gamma\gamma$ [51]. These pions originate from interactions of high-energy protons with ambient matter, such as the cold hydrogen background. However, the characteristic timescale for such hadronic interactions is significantly longer than the expected diffusive age of the UHE nebula (see Figure 24) [64]. Therefore, proton cooling can be considered negligible, which greatly simplifies subsequent estimates.

It should be noted, however, that inelastic pp collisions also produce charged pions, which decay into secondary electrons and positrons. These leptons may contribute to the overall gamma-ray output of the nebula via Inverse Compton. Moreover, neutrinos produced in these decays can be registered in modern neutrino telescopes (such as IceCube, KM3NeT, BaikalGVD, TRIDENT) and justify (or refute) hadronic component in the jet.

Secondary particles (γ, e^\pm) in inelastic pp interactions is calculated with the use of aafrag and aafragpy [65]. Figure 25 shows secondary gamma-ray spectra from monochromatic protons of 0.01, 1, and 100 PeV. It is important to note that peak photon energy in this processes is from 5 to 10% of the incident proton.

In order to estimate the probability of hadronic scenario, we look at hydrogen maps to identify potential overdensities and constrain cold proton density.

4.2. HI4PI Hydrogen Maps

The most recent and complete 3D hydrogen map is provided in HI4PI map based on EBHIS and GASS surveys [66]. The sky is divided into several *data cubes* of size $22^\circ \times 22^\circ$ in Galactic coordinates, the third dimension is given in radial velocity values from -600 to $+600$ km/s, which were measured from redshift of particular hydrogen emission lines. Positive radial velocities correspond to the objects, moving away from the observer.

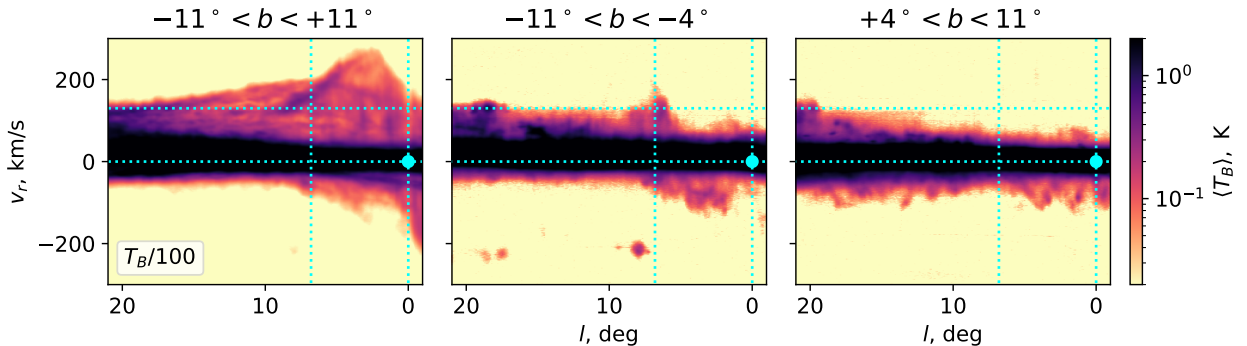


Figure 26: Average brightness temperature for centered, bottom and upper regions of the galactic plane in the data cube of interest. Blue lines indicate $b \in \{0^\circ; -6.8^\circ\}$; $v \in \{0; 130\}$ km/s.

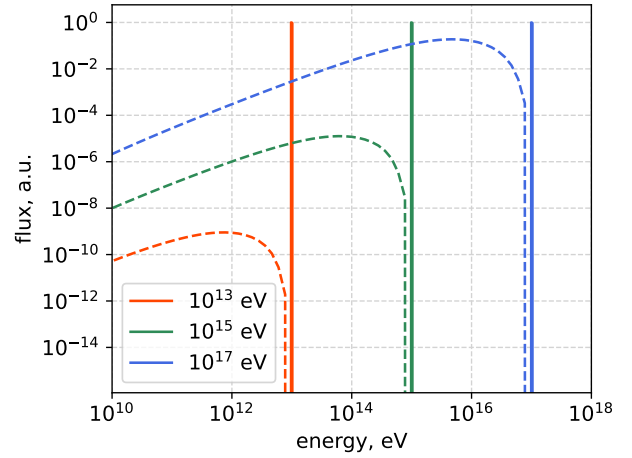


Figure 25: Secondary gamma-ray emission from monochromatic protons (0.01, 1, 100 PeV) in 1 cm^{-3} cold proton environment via aafrag [65].

It is important to note that peak photon energy in this processes is from 5 to 10% of the incident proton.

Figure 26 presents the brightness temperature profiles averaged over Galactic latitude b , for the full data cube (left panel), and separately for regions below -4° and above $+4^\circ$ (middle and right panel respectively). The source is situated within a band exhibiting a localized enhancement in brightness temperature associated with high-radial-velocity cold protons, reaching up to 200 km/s. This feature is absent at the corresponding longitude above the Galactic plane.

In Figure 27, we show the hydrogen column density in the vicinity of the source. For velocities $v \in [70; 76]$ km/s – matching the source’s systemic motion (see Table 3) – the distribution appears uniform, with no distinct anomalies. At higher velocities, potentially tracing gas dynamics influenced by the Galactic bar, a leg-like structure becomes apparent, extending from the Galactic center (0, 0) toward the source.

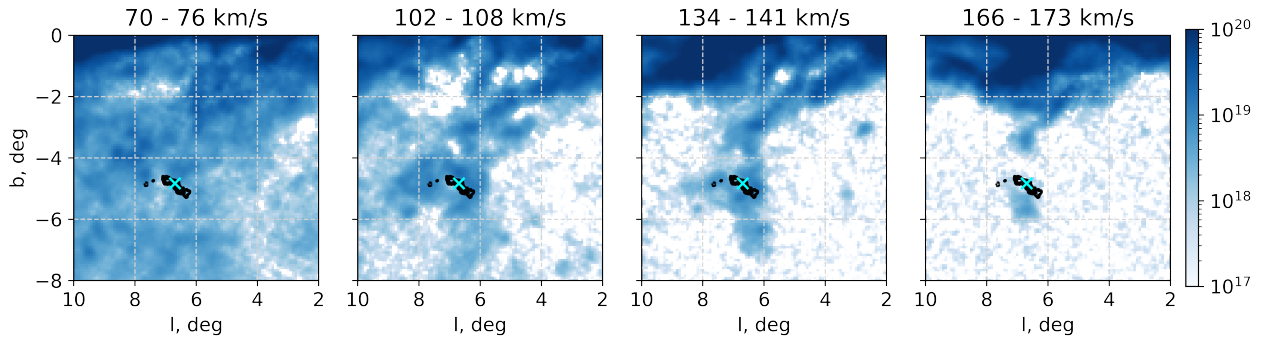


Figure 27: Column density (in g/cm^2) distribution in various velocity bands on the HI4PI hydrogen map. The location of V4641 Sgr is marked with a blue cross; semi-transparent red indicates H.E.S.S. significance contours.

As the source is located near the Galactic bar, the standard Milky Way rotation curve and the tangent-point method [41] are not applicable. Instead, we investigated gas hydrodynamical simulations within a Galactic potential composed of an axisymmetric disk, spiral arms, an ellipsoidal bar, and a bulge [67]. In the vicinity of the bar, gas undergoes significant perturbations and transitions from circular rotation to so-called x_1 - and x_2 -orbits [68, 69], which can be approximated, in the simplest form, by *aligned ellipses* [70] (see Figure 28).

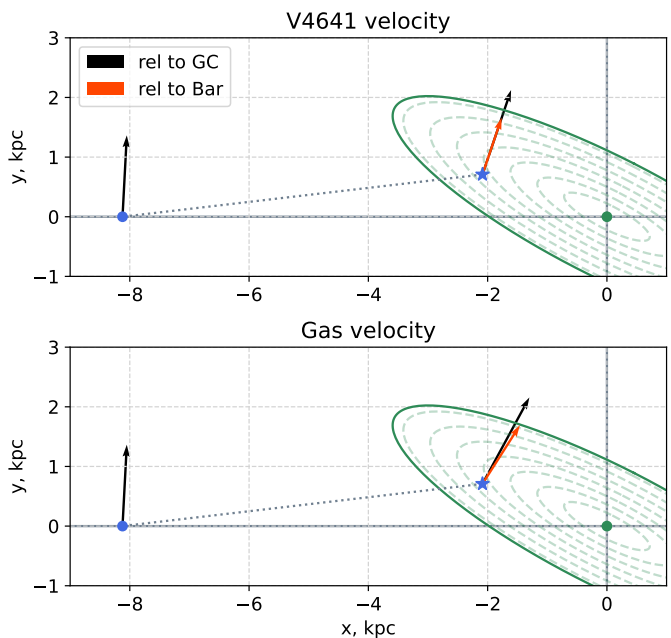


Figure 28: Velocities of the system.

By scanning through possible velocity values, we identified the velocity domain that best accounts for the nebula's asymmetry. The most promising pattern was found at $v = 130$ km/s and is shown in Figure 29. The Southern part of the source in the image is brighter, especially for higher energies, where the asymmetry in data is observed.

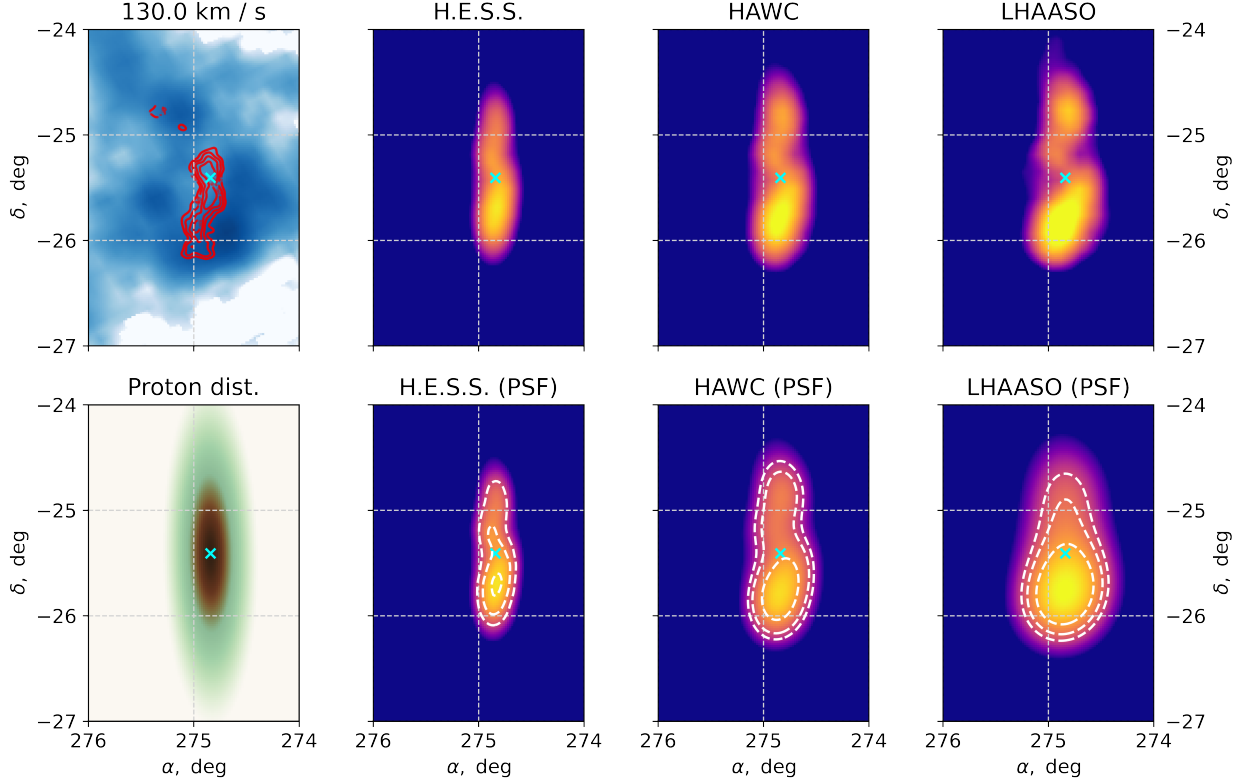


Figure 29: HI4PI proton density at $v = 130$ km/s in logarithmic scale (upper left), assumed proton density (bottom left), product of proton and HI densities for H.E.S.S., HAWC ($E > 100$ TeV), and LHAASO (upper row), and this product convolved with the point-spread functions of the corresponding detectors (bottom row). $T = 3260$ yr.

Therefore, cold proton maps observed in HI4PI contain an intrinsic asymmetry, which can be translated into the observed features of the nebula.

We next examine the gamma-ray filament spectra.

4.3. Proton Flash Scenario

As in the leptonic case, the simplest hadronic scenario involves a single proton flash. Figure 30 shows the MCMC sampling results, including secondary photon emission, synchrotron radiation for $B = 10 \mu\text{G}$, and the IC component from secondary electrons. These electrons are continuously produced by the high-energy proton population, leading to a growing IC contribution over time. However, as the system ages, electron cooling shifts the population to lower energies, leaving the 2–10 keV synchrotron band largely unaffected. At $10 \mu\text{G}$, this X-ray band corresponds to electrons with energies around 90 TeV.

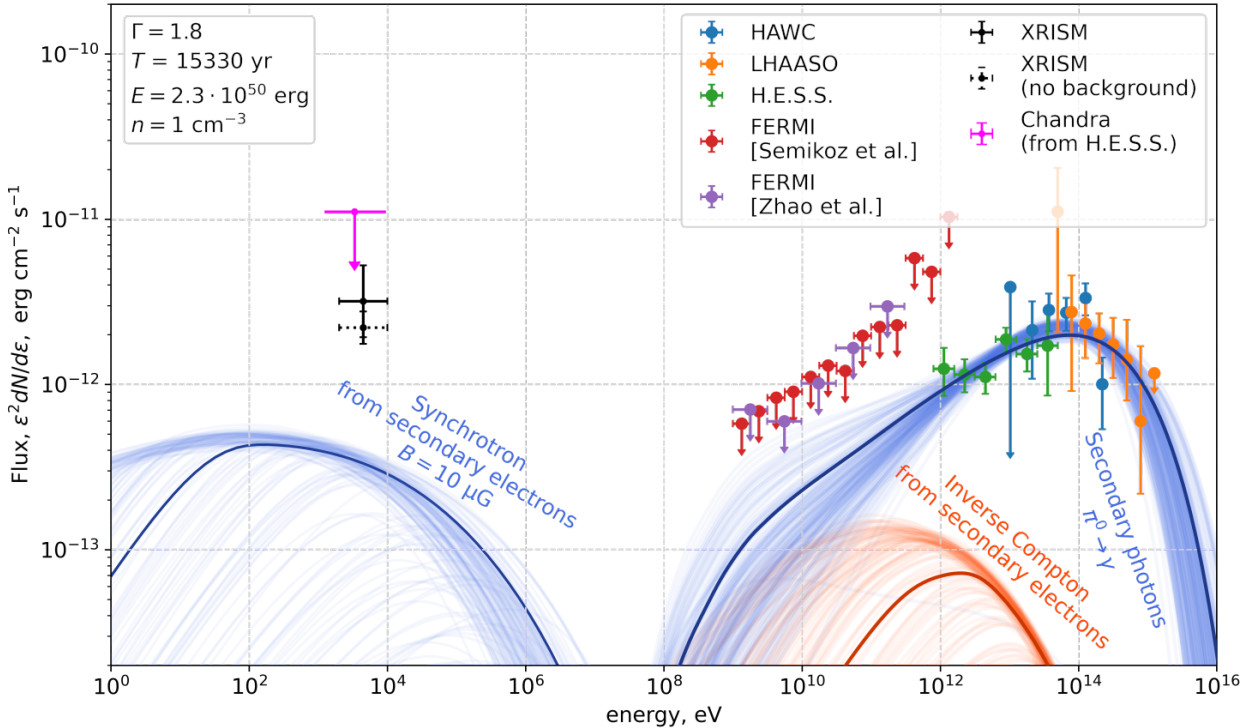


Figure 30: Single-flash proton model and corresponding gamma- and X-ray emission spectra for various lifetimes of the system. Secondary photons from inelastic pp interactions is shown in blue in the gamma-ray side of the picture, secondary electrons Inverse Compton and Synchrotron spectra are shown in red and blue respectively.

In Figure 30, we show a specific example of the hadronic spectrum with $\gamma = 1.8$ and $T = 15,330$ yr, assuming a density of $n = 1 \text{ cm}^{-3}$. The total energy required to sustain the proton nebula is estimated at $E \sim 2 \times 10^{50} \text{ erg}$ — about three orders of magnitude higher than in the leptonic scenario. Such an enormous release of energy in relativistic protons could only arise from a catastrophic event, such as the infall of a massive fragment of a companion star onto the black hole, or even a black hole formation event itself.

A scan over magnetic field values $B \in [1; 40] \mu\text{G}$ revealed no configuration in which the synchrotron component alone can reproduce the X-ray flux observed by XRISM. *This result admits two interpretations: either the single-flare hadronic model is insufficient to explain the data, or the XRISM signal originates from a different particle population — potentially thermal X-rays near the compact object.*

In the following subsections, we extend the hadronic model by introducing a leptonic component to account for the observed synchrotron emission.

4.4. Proton-Electron Flash

A minimal extension of the hadronic flash model introduces electrons produced in the same catastrophic event. Initially, their maximum energy is assumed equal to that of protons. However, electrons are subject to significant synchrotron – and to a lesser extent, Inverse Compton – cooling, which rapidly reduces their maximum energy over time.

To minimize the electron contribution while setting an upper limit on the flare age, we

consider the following. The maximum primary electron energy must dominate the synchrotron spectrum. Electrons radiating at 5 keV have energy $E = 270 \text{ TeV} (\mu\text{G}/B)^{1/2}$. Synchrotron cooling limits the maximum electron energy to $E < 1.3 \cdot 10^7 \text{ TeV} (\mu\text{G}/B)^2 (\text{yr}/T)$, which constrains the source lifetime as $T < 48 \text{ kyr} (B/\mu\text{G})^{-3/2}$.

Magnetic field also defines the magnitude of synchrotron emission, minimal field sufficient to reach XRISM value turns out to be $4\mu\text{G}$ for which the lifetime is less than 6 kyr.

Due to an increased amount of free parameters, we did not perform a MCMC sampling. Here we demonstrate a possibility to fit the observed gamma-ray spectrum with a peaked high-energy proton population with energies from 3 to 4 PeV and a $\gamma = 2.0$ electron distribution with a cut-off at 4 PeV. Scaled primary protons with ejected and cooled primary electrons and secondary contribution are presented in Figure 31.

Energetically, electrons were ejected with $E_e = 3 \cdot 10^{47} \text{ erg}$, protons with $E_p = 2.3 \cdot 10^{49} \text{ erg}$. As high-energy protons have approximately one-order larger diffusion coefficients, they

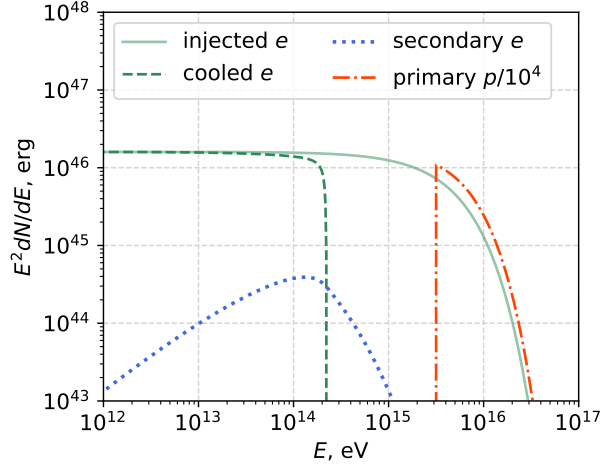


Figure 31: Electron and Photon spectra used to demonstrate the Proton-Electron flash model.

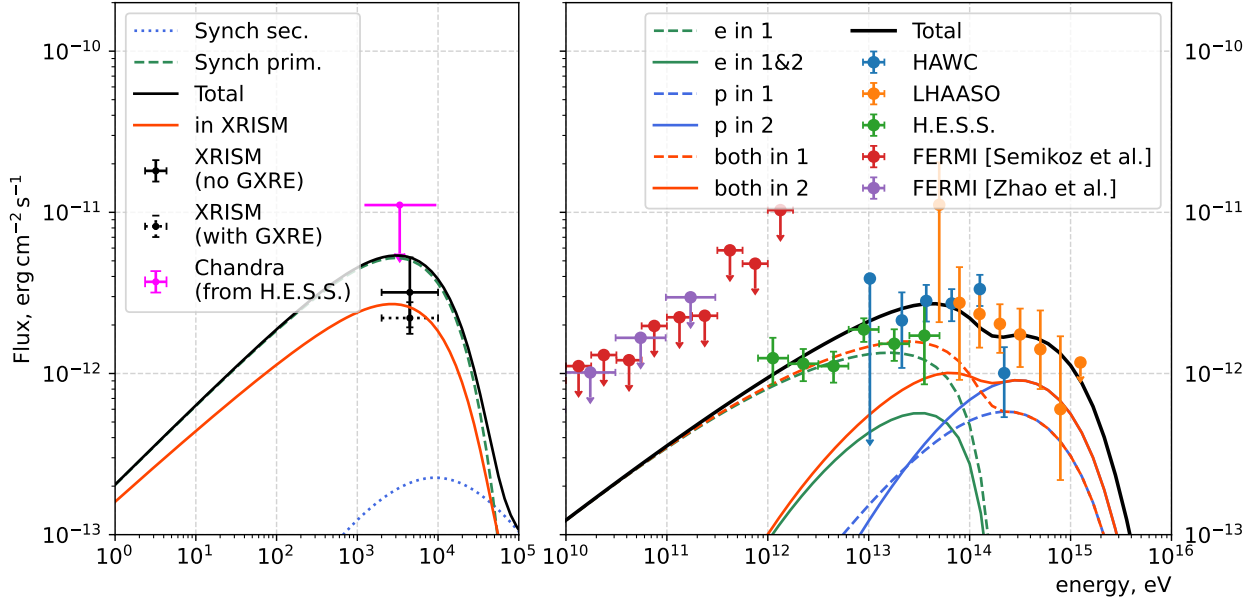


Figure 32: Synchrotron (left) and gamma-ray (gamma) radiation from the nebula and corresponding photon spectra in assumption of proton-electron flare. Dashed line on the right plot corresponds to the inner area ($d < 58 \text{ pc}$), the colored solid lines are drawn for the outer area ($d > 58 \text{ pc}$). The age of the flare is 3260 yr.

travel several times further than electrons. In this case, we can split the total area of the nebula into two parts: $r < 58$ pc (corresponds to H.E.S.S. contours), and $r > 58$ pc, which contains only HAWC > 100 TeV and LHAASO tails. Figure 32 shows simultaneously fitted synchrotron and high-energy emission, where the latter is split between two areas.

We conclude that the proton-electron scenario adequately explains both spectral and morphological features of the nebula, but note that the unusual proton ejection spectrum implies a highly specific acceleration mechanism.

4.5. Proton Flash and Electron Emission

To weaken the synchrotron radiation constraints, we can assume electrons are periodically injected to the nebula in 1999-like flares of the binary. Thus, we would combine constant emission electron model with a proton flash.

Identically to the proton-electron flash scenario, we only demonstrate a possibility to fit data under this assumption. The corresponding spectra are introduced in Figure 34. This scenario allows to use a much simpler proton spectrum with $\gamma = 1.4$, $E_{\text{cut}} = 5$ PeV, and $E = 1.2 \cdot 10^{50}$ erg.

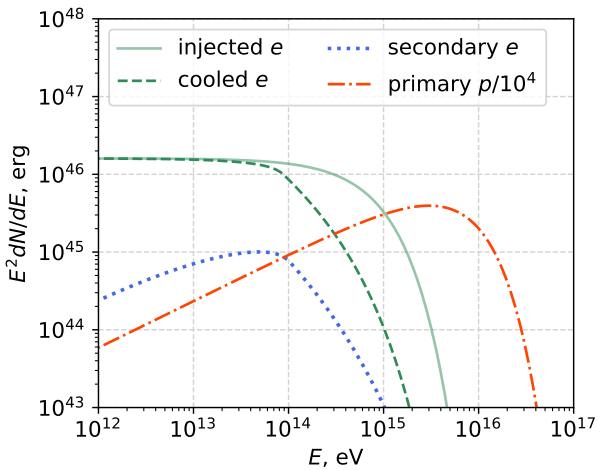


Figure 34: Electron and Photon spectra used to demonstrate the Proton-Electron flash model.

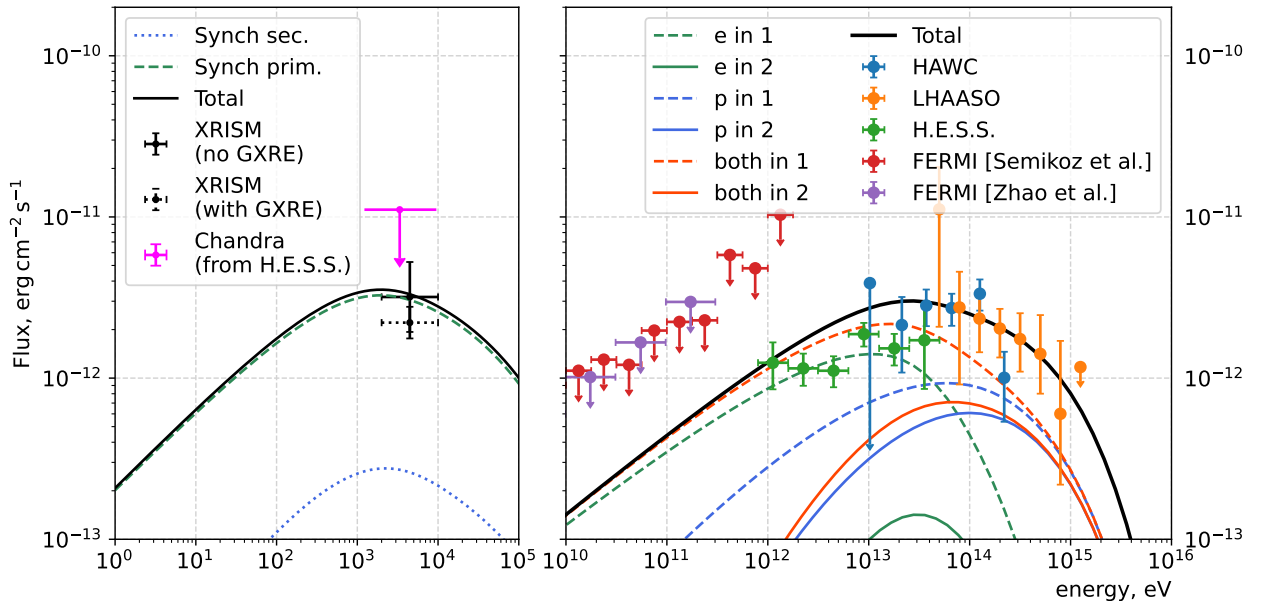


Figure 33: Synchrotron (left) and gamma-ray (right) radiation from the nebula and corresponding photon spectra in assumption of proton flare accompanied by continuous electron emission. Dashed line on the right plot corresponds to the inner area ($d < 58$ pc), the colored solid lines are drawn for the outer area ($d > 58$ pc.) The age of the flare is 7360 yr, magnetic field is 4 μ G.

Electrons are ejected with $\gamma = 2.0$, $E_{\text{cut}} = 600 \text{ TeV}$, $L = 1.7 \cdot 10^{36} \text{ erg/s}$.

Figure 33 presents the synchrotron emission, now concentrated near the source due to continuous electron injection (left panel). The gamma-ray component is shown in the right panel, separated into inner and outer zones. The dashed red line, representing photons from electrons and protons in the inner region, fits well the H.E.S.S. data and lower-energy HAWC measurements. The HAWC $> 100 \text{ TeV}$ and LHAASO points extend into the outer region and are described by the black curve, which accounts for the total gamma-ray flux from the source.

Both the proton–electron flare and the current model are designed such that the low-energy portion of the spectrum is explained by inverse Compton scattering from electrons, while the highest energies originate from π^0 decay.

The proton flash accompanied by electron emission explains the spectral and morphological properties of the filament and is favored as it permits a longer flash age.

Summary

In this section, we examined three hadronic models based on diffusive cosmic-ray transport. Diffusion along the regular component of the Galactic magnetic field explains the source elongation and its energy-dependent morphology, while the observed asymmetry is attributed to background cold proton density at $v = 130 \text{ km/s}$.

1. The single-flash hadronic model reproduces the gamma-ray spectrum well but fails to account for the extended X-ray emission observed by XRISM.
2. The proton–electron flash scenario, which assumes a single hadro-leptonic ejection event, is constrained by $T < 48 \text{ kyr} (B/\mu\text{G})^{-3/2}$ and requires a magnetic field of $\sim 4 \mu\text{G}$ to reproduce both the diffusion profile and synchrotron emission. However, it is disadvantaged by the narrow shape of the required proton injection spectrum, confined to 2-10 PeV.
3. The proton flash model with continuous electron injection offers the most flexibility in choosing injection spectra. A magnetic field of $4 \mu\text{G}$ is sufficient to reproduce both the synchrotron data and the observed nebula morphology.

Compared to the leptonic scenario, the proton-flash model requires a significantly higher total energy release, $E \sim 10^{50} \text{ erg}$, which could be injected into protons only during a recent catastrophic event—such as the infall of a large portion of the companion star onto the black hole, or the very formation of the black hole from a massive progenitor.

5. Results and Discussion

As shown, the gamma-ray nebula surrounding V4641 Sgr exhibits several nontrivial spectral and morphological features. In this work, we constructed phenomenological leptonic and hadronic models to describe the observed filament. To simplify the analysis, we treated the nebula's morphology and energetics separately.

To investigate the morphological characteristics, we examined three transport scenarios — ballistic, diffusive, and mixed — assuming that high-energy particles propagate along regular Galactic magnetic field lines, as proposed in [29]. Each scenario was adapted to the corresponding spectral models to account for key observational features: energy-dependent filament length, finite transverse width, and the pronounced North-South asymmetry at energies above 100 TeV.

As the less energetically demanding option, leptonic scenarios were addressed first in section 3. In these models, high-energy gamma rays are produced via inverse Compton scattering on background radiation fields (primarily the CMB and thermal dust emission), while X-rays result from synchrotron radiation emitted by electrons in the Galactic magnetic field.

We have identified the following cases:

- A single-flash electronic scenario, which fits X-Ray measurements for $B \simeq 5 \mu\text{G}$, and thus has a short lifetime of $< 500 \text{ yr}$, which allows for ballistic transport model only. It also requires a major flash of $\sim 10^{47} \text{ erg}$ a short time ago, an event that would likely have been observed from Earth. We therefore consider this scenario disfavored.
- A continuous emission scenario due to a different transport profile, allows to accommodate lower magnetic fields $> 2 \mu\text{G}$ while still fitting the observed synchrotron X-ray flux. We disfavor a steady-state injection due to the high luminosity requirements, which are inconsistent with recent observations. A time-limited continuous injection over 3-10 kyr offers a viable, self-consistent model. It also provides two plausible mechanisms for the observed morphology: bending of a regular magnetic field line, or a transition from ballistic to diffusive propagation at higher energies.

As the morphological assumptions in leptonic models remain somewhat speculative, we also consider three hadronic scenarios. These models are generally favored from a theoretical standpoint, as they offer a plausible explanation for the origin of galactic cosmic rays above the knee — a long-standing open question in astrophysics. In hadronic models, high-energy photons arise from $pp \rightarrow \pi^0 \rightarrow \gamma\gamma$ interactions.

- The single-flash proton scenario fails to reproduce the X-ray emission for magnetic fields $B \in [1, 40] \mu\text{G}$, as the resulting secondary electrons are insufficient to account for the observed synchrotron radiation. This scenario is disfavored unless the X-ray emission is confirmed to be of thermal origin.
- Introducing a leptonic component, the proton-lepton flash model yields a satisfactory spectral fit. However, it requires an unrealistically narrow proton energy distribution centered at a few PeV, which challenges its physical plausibility.

- The proton flash with continuous electron emission scenario alleviates the above constraints and successfully reproduces both gamma-ray and X-ray spectra, making it the most consistent among the hadronic models considered.

Compared to leptonic models, hadronic scenarios demand an enormous energy release during the flash ($> 10^{50}$ erg), likely attainable only through a catastrophic event—such as the accretion of a substantial fraction of the companion star or the black hole’s formation from a massive progenitor.

However, unlike leptonic cases, hadronic models naturally account for the observed source asymmetry through variations in the ambient gas density, as revealed by 3D ionized hydrogen maps.

Based on our results, we propose a straightforward *observational test to distinguish between the discussed scenarios*. In leptonic models, the Southern edge of the gamma-ray nebula is populated by the highest-energy electrons, which emit via inverse Compton scattering. These same electrons are expected to produce synchrotron radiation extending into the hard X-ray range (100–1000 keV in a $2 \mu\text{G}$ magnetic field). In contrast, hadronic models localize electrons closer to the binary, within the H.E.S.S. detection region, implying a predominantly hadronic origin of the high-energy emission and a suppressed synchrotron signal in the X-ray band at the nebula tip.

An alternative discriminant involves the search for high-energy neutrinos from the source using detectors such as IceCube, KM3NeT, Baikal-GVD, or TRIDENT. However, as shown in [29], the predicted neutrino flux is low, making X-ray observations a more practical and immediate avenue for constraining the emission mechanism.

Planned developments

While the qualitative aspects of the proposed models are established, several technical steps remain to finalize the quantitative predictions. In the case of the single-flash leptonic scenario, the X-ray flux has already been properly rescaled to account for the limited field of view of XRISM. For the continuous emission and especially the ballistic-diffusive transport profiles, the propagation models are more complex and still require consistent rescaling to validate the results. Furthermore, the lepto-hadronic scenarios should be subjected to MCMC sampling in order to identify the most probable spectral configurations.

Acknowledgments

I would like to express my sincere gratitude to Dr. Dmitri Semikoz, my scientific advisor, for his constant support, readiness to help, and insightful guidance throughout this work. I am also deeply thankful to Dr. Foteini Oikonomou for her valuable assistance with photon production mechanisms and for suggesting effective approaches to verify my results. Special thanks go to Dr. Andrii Neronov, whose thoughtful comments and participation in discussions led to several important — and at times unexpected — developments in this research.

References

- [1] Kachelrieß, M. and Semikoz, D. “Cosmic ray models”. *Progress in Particle and Nuclear Physics* 109 (Nov. 2019), p. 103710. [DOI](#).
- [2] Longair, M.S. *High Energy Astrophysics*. Cambridge: Cambridge University Press, Feb. 2011.
- [3] Cao, Z. et al. “Ultra-High-Energy Gamma-Ray Astronomy”. *Annual Review of Nuclear and Particle Science* 73.1 (Sept. 2023), pp. 341–363. [DOI](#).
- [4] Alfaro, R. et al. “Ultra-high-energy gamma-ray bubble around microquasar V4641 Sgr”. *Nature* 634.8034 (Oct. 2024), pp. 557–560. [DOI](#).
- [5] LHAASO Collaboration. “Ultrahigh-energy gamma-ray emission associated with black hole-jet systems” (2024). [arXiv](#).
- [6] Olivera-Nieto, L. “H.E.S.S. detection of very high energy emission surrounding the microquasar V4641 Sgr”. 2024.
- [7] Hjellming, R.M. et al. “Light curves and radio structure of the 1999 September transient event in V4641 sagittarii”. *Astrophys. J.* 544.2 (Dec. 2000), pp. 977–992. [DOI](#).
- [8] Revnivtsev, M. et al. “Super-Eddington outburst of V4641 sgr”. *Astron. Astrophys.* 391.3 (Sept. 2002), pp. 1013–1022.
- [9] Suzuki, H. et al. “Detection of Extended X-Ray Emission around the PeVatron Microquasar V4641 Sgr with XRISM”. *Astrophys. J. Lett.* 978.2 (Jan. 2025), p. L20. [DOI](#).
- [10] Gaia Collaboration et al. “Gaia Data Release 3”. *Astron. Astrophys.* 674 (June 2023).
- [11] Wenger, M. et al. “The SIMBAD astronomical database. The CDS reference database for astronomical objects”. *Astronomy and Astrophysics Supplement* 143 (Apr. 2000), pp. 9–22. [DOI](#).
- [12] Ochsenbein, F., Bauer, P., and Marcout, J. “The VizieR database of astronomical catalogues”. *Astronomy and Astrophysics Supplement* 143 (Apr. 2000), pp. 23–32. [DOI](#).
- [13] European Space Agency, ed. *The HIPPARCOS and TYCHO catalogues. Astrometric and photometric star catalogues derived from the ESA HIPPARCOS Space Astrometry Mission*. Vol. 1200. ESA Special Publication. Jan. 1997.
- [14] Ginsburg, A. et al. “astroquery: An Astronomical Web-querying Package in Python”. *Astron. J.* 157.3 (Feb. 2019), p. 98. [DOI](#).
- [15] Uemura, M. et al. “The 1999 optical outburst of the fast X-ray Nova, V4641 sagittarii”. *Publ. Astron. Soc. Jpn. Nihon Tenmon Gakkai* 54.1 (Feb. 2002), pp. 95–101. [DOI](#).
- [16] Barsukova, E.A., Goranskij, V.P., and Kroll, P. *Historical light curve of the black hole binary V4641 Sgr based on the Moscow and Sonneberg plate archives*. 2014. [arXiv](#).
- [17] Kato, T. et al. *Preoutburst Activity of V4641 Sgr = SAX J1819.3-2525: Possible Existence of 2.5-Day Period*. Oct. 1999.
- [18] Stubbings, R. *V4641 Sgr — X-Ray Binary Black Hole Star System*. Accessed: 2025-05-16. [link](#).
- [19] NASA. *RXTE Discoveries*. Accessed: 2025-05-16. [link](#).
- [20] *The Astronomer’s Telegram*. Accessed: 2025-07-08. [link](#).
- [21] MacDonald, R.K.D. et al. “The black hole binary V4641 Sagitarii: Activity in quiescence and improved mass determinations”. *Astrophys. J.* 784.1 (Feb. 2014), p. 2. [DOI](#).
- [22] Pandey, M. et al. “Low-frequency radio monitoring of microquasars”. *Astron. Astrophys.* 463.2 (Feb. 2007), pp. 567–577. [DOI](#).
- [23] Miller-Jones, J.C.A. et al. “A deep radio survey of hard state and quiescent black hole x-ray binaries”. *Astrophys. J. Lett.* 739.1 (Sept. 2011), p. L18. [DOI](#).
- [24] Chaty, S. et al. “Optical and near-infrared observations of the microquasar V4641 Sgr during the 1999 September outburst”. *Mon. Not. R. Astron. Soc.* 343.1 (July 2003), pp. 169–174. [DOI](#).
- [25] Orosz, J.A. et al. “A black hole in the superluminal source SAX J1819.3-2525 (V4641 sgr)”. *Astrophys. J.* 555.1 (July 2001), pp. 489–503. [DOI](#).
- [26] Connors, R.M.T. et al. “Reprocessing from highly ionized gas in the soft spectral state of V4641 Sgr with NuSTAR”. *Astrophys. J.* 983.1 (Apr. 2025), p. 25. [DOI](#).

- [27] Pahari, M. et al. “Constraining the Distance and Inclination Angle of V4641 Sgr Using Swift and NuSTAR Observations During the Low Soft Spectral State”. *Astrophys. J.* 814.2 (Dec. 2015), p. 158. [DOI](#).
- [28] Tomsick, J.A. et al. “Chandra Detections of Two Quiescent Black Hole X-Ray Transients”. *The Astrophysical Journal* 597.2 (Oct. 2003), pp. L133–L136. [DOI](#).
- [29] Neronov, A., Oikonomou, F., and Semikoz, D. “Multi-messenger signature of cosmic rays from the microquasar V4641 Sgr propagating along a Galactic Magnetic Field line” (2024). [arXiv](#).
- [30] Zhao, Z., Li, J., and Torres, D.F. “Upper limits on the gamma-ray emission from the microquasar V4641 Sgr” (2025). [arXiv](#).
- [31] Smith, D.A., Levine, A.M., and Morgan, E.H. *V4641 Sagittarii*. IAU Circular. <https://cbat.eps.harvard.edu/iauc/07200/07253.html>. 1999.
- [32] Lindstrøm, C. et al. “New clues on outburst mechanisms and improved spectroscopic elements of the black hole binary V4641 Sagittarii*”. en. *Mon. Not. R. Astron. Soc.* 363.3 (Nov. 2005), pp. 882–890.
- [33] Salvesen, G. and Pokawanvit, S. “Origin of spin–orbit misalignments: the microblazar V4641 Sgr”. *Mon. Not. R. Astron. Soc.* 495.2 (June 2020), pp. 2179–2204.
- [34] Gaia Collaboration et al. “Gaia Data Release 2”. *Astron. Astrophys.* 616 (Aug. 2018), A1.
- [35] Salvesen, G. and Pokawanvit, S. “Origin of spin–orbit misalignments: the microblazar V4641 Sgr”. *Mon. Not. R. Astron. Soc.* 495.2 (June 2020), pp. 2179–2204. [DOI](#).
- [36] Miller, J.M. et al. “A Relativistic Fe K α Emission Line in the Intermediate-Luminosity BeppoSAX Spectrum of the Galactic Microquasar V4641 Sgr”. *The Astrophysical Journal* 577.1 (Sept. 2002), pp. L15–L18. [DOI](#).
- [37] Muñoz-Darias, T., Torres, M.A.P., and Garcia, M.R. “The low-luminosity accretion disc wind of the black hole transient V4641 Sagittarii”. *Monthly Notices of the Royal Astronomical Society* 479.3 (2018). [DOI](#).
- [38] Portail, M. et al. “Dynamical modelling of the galactic bulge and bar: the Milky Way’s pattern speed, stellar and dark matter mass distribution”. *Monthly Notices of the Royal Astronomical Society* 465.2 (Nov. 2016), pp. 1621–1644. [DOI](#).
- [39] Wegg, C., Gerhard, O., and Portail, M. “The structure of the Milky Way’s bar outside the bulge”. *Monthly Notices of the Royal Astronomical Society* 450.4 (May 2015), pp. 4050–4069. [DOI](#).
- [40] Bland-Hawthorn, J. and Gerhard, O. “The Galaxy in Context: Structural, Kinematic, and Integrated Properties”. *Annual Review of Astronomy and Astrophysics* 54.1 (Sept. 2016), pp. 529–596. [DOI](#).
- [41] Chemin, L., Renaud, F., and Soubiran, C. “Incorrect rotation curve of the Milky Way”. *Astronomy & Astrophysics* 578 (May 2015), A14. [DOI](#).
- [42] Lucey, M. et al. “Dynamically constraining the length of the Milky way bar”. *Monthly Notices of the Royal Astronomical Society* 520.3 (Feb. 2023), pp. 4779–4792. [DOI](#).
- [43] Collaboration, T.A. et al. “The Astropy Project: Sustaining and Growing a Community-oriented Open-source Project and the Latest Major Release (v5.0) of the Core Package*”. *The Astrophysical Journal* 935.2 (Aug. 2022), p. 167. [DOI](#).
- [44] Popescu, C.C. et al. “A radiation transfer model for the Milky Way: I. Radiation fields and application to high-energy astrophysics”. *Monthly Notices of the Royal Astronomical Society* 3 (May 2017), pp. 2539–2558. [DOI](#).
- [45] Misiriotis, A. et al. “The distribution of the ISM in the Milky Way: A three-dimensional large-scale model”. *Astronomy & Astrophysics* 459.1 (Sept. 2006), pp. 113–123. [DOI](#).
- [46] Ferrière, K., Gillard, W., and Jean, P. “Spatial distribution of interstellar gas in the innermost 3 kpc of our galaxy”. *Astronomy & Astrophysics* 467.2 (Feb. 2007), pp. 611–627. [DOI](#).
- [47] H.E.S.S. Collaboration*† et al. “Acceleration and transport of relativistic electrons in the jets of the microquasar SS 433”. en. *Science* 383.6681 (Jan. 2024), pp. 402–406.
- [48] Abeysekara, A.U. et al. *Observation of the crab nebula with the HAWC gamma-ray observatory*. June 2017.

- [49] Vernetto, S. and Lipari, P. "Absorption of very high energy gamma rays in the Milky Way". *Phys. Rev. D* 94 (6 Sept. 2016), p. 063009. [DOI](#).
- [50] Jokipii, J.R. "Cosmic-ray propagation. I. charged particles in a random magnetic field". en. *Astrophys. J.* 146 (Nov. 1966), p. 480.
- [51] Ginzburg, V.L. and Syrovatskii, S.I. "The Origin of Cosmic Rays". Russian. Moscow: Academy of Sciences of the USSR, 1963. Chap. 3.
- [52] Giacinti, G., Kachelriess, M., and Semikoz, D.V. "Reconciling cosmic ray diffusion with Galactic magnetic field models". *J. Cosmol. Astropart. Phys.* 2018.07 (July 2018), pp. 051–051.
- [53] Shalchi, A. *Nonlinear Cosmic Ray Diffusion Theories*. Vol. 362. 2009. Chap. 2 and 3. [DOI](#).
- [54] Marco, D.D., Blasi, P., and Stanev, T. "Numerical propagation of high energy cosmic rays in the Galaxy: I. Technical issues". *Journal of Cosmology and Astroparticle Physics* 2007.06 (June 2007), pp. 027–027. [DOI](#).
- [55] Mertsch, P. "Test particle simulations of cosmic rays". *Astrophysics and Space Science* 365.8 (Aug. 2020). [DOI](#).
- [56] Giacinti, G., Kachelrieß, M., and Semikoz, D.V. "Filamentary Diffusion of Cosmic Rays on Small Scales". *Physical Review Letters* 108.26 (June 2012). [DOI](#).
- [57] Xiao, Y., Zhang, J., and Xu, S. *Studying the diffusion mechanism of cosmic-ray particles*. 2025. [arXiv](#).
- [58] Gombosi, T.I. et al. "The Telegraph Equation in Charged Particle Transport". *Astrophysical Journal* 403 (Jan. 1993), p. 377. [DOI](#).
- [59] Litvinenko, Y.E. and Schlickeiser, R. "The telegraph equation for cosmic-ray transport with weak adiabatic focusing". *Astron. Astrophys.* 554 (June 2013), A59. [DOI](#).
- [60] Tautz, R.C. and Lerche, I. "Application of the three-dimensional telegraph equation to cosmic-ray transport". *Res. Astron. Astrophys.* 16.10 (Oct. 2016), p. 162. [DOI](#).
- [61] Blumenthal, G.R. and Gould, R.J. "Bremsstrahlung, Synchrotron Radiation, and Compton Scattering of High-Energy Electrons Traversing Dilute Gases". *Rev. Mod. Phys.* 42 (2 Apr. 1970), pp. 237–270. [DOI](#).
- [62] Kalashev, O. et al. "Modeling the propagation of very-high-energy γ -rays with the CRbeam code: Comparison with CRPropa and ELMAG codes". *Astron. Astrophys.* 675 (July 2023), A132.
- [63] Fouka, M. and Ouichaoui, S. "Analytical fits to the synchrotron functions". 13.6 (June 2013), pp. 680–686.
- [64] Cudell, J.R. et al. "Benchmarks for the Forward Observables at RHIC, the Tevatron-Run II, and the LHC". *Physical Review Letters* 89.20 (Oct. 2002). [DOI](#).
- [65] Koldobskiy, S. et al. "Energy spectra of secondaries in proton-proton interactions". *Phys. Rev. D* 104 (12 Dec. 2021), p. 123027. [DOI](#).
- [66] Ben Bekhti, N. et al. "HI4PI: a full-sky HI survey based on EBHIS and GASS". *Astronomy & Astrophysics* 594 (Oct. 2016), A116. [DOI](#).
- [67] Li, Z. et al. "Gas Dynamics in the Galaxy: Total Mass Distribution and the Bar Pattern Speed". *The Astrophysical Journal* 925.1 (Jan. 2022), p. 71. [DOI](#).
- [68] Lindblad, P.O. and Lindblad, P.A.B. "Kinematics of Interstellar Matter in a Barred Potential in the Epicyclic Approximation". *Physics of the Gaseous and Stellar Disks of the Galaxy*. Ed. by I.R. King. Vol. 66. Astronomical Society of the Pacific Conference Series. 1994, p. 29.
- [69] Regan, M.W. and Teuben, P. "The Formation of Nuclear Rings in Barred Spiral Galaxies". *The Astrophysical Journal* 582.2 (Jan. 2003), pp. 723–742. [DOI](#).
- [70] Liu, J., Li, Z., and Shen, J. "The Impact of Bar-induced Noncircular Motions on the Measurement of Galactic Rotation Curves". *The Astrophysical Journal* 980.1 (Feb. 2025), p. 146. [DOI](#).

Appendices

A. Solving the Diffusion Equation

A.1. From Anisotropic to Isotropic Diffusion Equation

To describe behavior of particles in a turbulent magnetic field $\delta\mathbf{B}$ with a regular component \mathbf{B}_0 , one can use anisotropic diffusion equation

$$\partial_t n(\mathbf{r}, t) - \partial_i D^{ik} \partial_k n(\mathbf{r}, t) = q(\mathbf{r}, t). \quad (\text{A.1})$$

Straight Regular Component

If the regular field is directed along a straight line, one can introduce a MF-related cartesian coordinate system (ξ, η, ζ) , where ξ is the line-of-sight, η is aligned with \mathbf{B}_0 , and ζ is the third axis in a right-handed triplet. In these coordinates the diffusion tensor D^{ik} is diagonal: $D^{ik} = \text{diag}(D_{||}, D_{\perp}, D_{\perp})$.

By rescaling the coordinates

$$\begin{aligned}\xi' &= \xi \sqrt{D_{||}/D_{\perp}}, \\ \eta' &= \eta, \\ \zeta' &= \zeta \sqrt{D_{||}/D_{\perp}},\end{aligned}$$

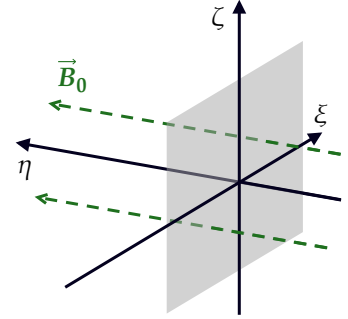


Figure 35: Axes ξ, η, ζ in relation to regular magnetic field \mathbf{B}_0 .

(A.1) is transformed into an isotropic diffusion equation (A.2) in primed coordinates (hereinafter, the primes are omitted).

$$\frac{\partial n}{\partial t}(\mathbf{r}, t) - D_{||} \Delta n(\mathbf{r}, t) = q(\mathbf{r}, t) \quad (\text{A.2})$$

Curved Regular Component

If regular magnetic field lines are curved, the diffusion tensor is space-dependent and can be obtained from the diagonal matrix $D = \text{diag}(D_{||}, D_{\perp}, D_{\perp})$ by rotation matrix $J(\mathbf{r})$:

$$D^{ik}(\mathbf{r}) = J_\alpha^i(\mathbf{r}) J_\beta^k(\mathbf{r}) D^{\alpha\beta}.$$

In this case, from (A.1) one cannot go directly to (A.2). Instead we get

$$\partial_t n(\mathbf{r}, t) - \partial_i D^{ik}(\mathbf{r}) \partial_k n(\mathbf{r}, t) = q(\mathbf{r}, t). \quad (\text{A.3})$$

By reverting the transformation $r'^\gamma = J_i^\gamma r^i$, we obtain $\partial_i = (J^{-1})_i^\gamma \partial'_\gamma$ and hence

$$\partial_t n(\mathbf{r}, t) - D^{\alpha\beta} (J^{-1})_i^\gamma \partial'_\gamma J_\alpha^i \partial'_\beta n(\mathbf{r}, t) = q(\mathbf{r}, t).$$

If we assume that the characteristic diffusion scale L_{dif} is much smaller than the magnetic field bending scale R_B , the rotation matrix $J_\alpha^i(\mathbf{r})$ can be written as $J_\alpha^i(\mathbf{r}) \simeq \delta_\alpha^i + \frac{L_{\text{dif}}}{R_B} M_\alpha^i$, and in the zero order we arrive again to (A.2) written in the new coordinate system.

A.2. Method of Green's Function

General Formulation for the Diffusion Equation

In previous subsection, we showed that in our case it is enough to solve the isotropic diffusion equation (A.2). We use the method of Green's Function to obtain a solution of the Cauchy problem

$$\frac{\partial n}{\partial t}(\mathbf{r}, t) - D_{\parallel} \Delta n(\mathbf{r}, t) = q(\mathbf{r}, t), \quad n(\mathbf{r})|_{t=t_0} = 0. \quad (\text{A.4})$$

Green's function method allows constructing a solution as a convolution of the ejection term with the *Green's function* $G(t, t'; \mathbf{r}, \mathbf{r}')$, which is a solution for

$$(\partial_t - D_{\parallel} \Delta) G(t, t'; \mathbf{r}, \mathbf{r}') = \delta(t - t') \delta^{(3)}(\mathbf{r} - \mathbf{r}'). \quad (\text{A.5})$$

Due to temporal and spatial translational invariance of the left-hand part, the Green's function is reduced to $G(t - t', \mathbf{r} - \mathbf{r}')$. Equation (A.5) has a well-known solution [71]

$$G(\tau, \boldsymbol{\rho}) = \frac{1}{(4\pi D_{\parallel} \tau)^{3/2}} \exp\left\{-\frac{\boldsymbol{\rho}^2}{4D_{\parallel} \tau}\right\}. \quad (\text{A.6})$$

With the Green's function, the solution for (A.4) can be computed from

$$n(\mathbf{r}, t) = \int_{t_0}^t dt' \int d^3 \mathbf{r}' G(\mathbf{r} - \mathbf{r}', t - t') q(\mathbf{r}', t'). \quad (\text{A.7})$$

Constant Ejection from a Point-Source

In the following discussion, we focus on the ejection that began at $t = 0$, lasted until $t = T$, and is observed at times $t \geq T$.

We assume that the ejection was point-like and time-independent at $0 \leq t \leq T$, so the corresponding Cauchy problem is

$$\begin{cases} \partial_n(\mathbf{r}, t) - D \Delta n(\mathbf{r}, t) = Q \delta^{(3)}(\mathbf{r}) \cdot \mathbf{1}(0 \leq t \leq T), \\ n(\mathbf{r}, 0) = 0. \end{cases} \quad (\text{A.8})$$

This problem has a straightforward solution derived from the Green's function of the heat (diffusion) equation [71], which appears spherically symmetric in primed coordinates

$$n(\mathbf{r}, t) = \frac{Q}{4\pi D_{\parallel} r} \left[\operatorname{erf}\left(\frac{r}{\sqrt{4D(t-T)}}\right) - \operatorname{erf}\left(\frac{r}{\sqrt{4Dt}}\right) \right]. \quad (\text{A.9})$$

Limiting Cases

1. *Continuous ejection: $t = T$.*

At $t = T$ we use $\lim_{\xi \rightarrow \infty} \operatorname{erf}(\xi) = 1$ and obtain

$$n(r, t) = \frac{Q}{4\pi D r} \operatorname{erfc}\left(\frac{r}{\sqrt{4Dt}}\right)$$

2. *Steady-state ejection*: $t = T \gg r/\sqrt{4D}$.

Here we use $\lim_{\xi \rightarrow 0} \operatorname{erfc}(\xi) = 1$ and get the famous Poisson's equation solution

$$n(r) = \frac{Q}{4\pi Dr}.$$

3. *Flare-like single ejection*: $t \gg T$.

In this case we refer to the fact that

$$\frac{d}{d\xi} \operatorname{erf}(\xi) = \frac{2}{\sqrt{\pi}} e^{-\xi^2} \text{ and get}$$

$$n(r, t) \simeq \frac{QT}{(4\pi Dt)^{3/2}} \exp\left\{-\frac{r^2}{4Dt}\right\}$$

4. *Long-ago single ejection*: $t \gg r/\sqrt{4D} \gg T$.

By using a standard decomposition of an exponent $e^{-\xi} \simeq 1 - \xi$ we obtain

$$n(r, t) \simeq \frac{QT}{(4\pi Dt)^{3/2}} \left(1 - \frac{r^2}{4Dt}\right).$$

A.3. Projected intensity map

All observable features of the source are represented as a flat projection onto the two-dimensional celestial sphere, which is locally approximated as a plane. In this case, one sees only the projection of the source onto the Oxz plane. In assumption that radiation intensity I is proportional to local high-energy particle density (electrons or protons), we write

$$I(x, z) \propto \int dy n(r(x, y, z), t_{\text{obs}}).$$

The H.E.S.S. Collaboration [6] showed preliminary 1D-measurements of the intensity along the nebula (z -axis). To obtain the 1D-projected intensity distribution, one performs integration along x and z axes:

$$I(z) \propto \int dx dy n(r(x, y, z), t_{\text{obs}}).$$

In case of diffusion along straight MF lines (A.9), the projection formula is analytical and is given by (A.10), which allows for setting constraints on ejection parameters Dt and $D(t - T)$.

$$I(z) \propto \frac{QT}{2\sqrt{\pi DT}} \left[\sqrt{4Dt} \exp\left\{-\frac{z^2}{4Dt}\right\} - \sqrt{4D(t-T)} \exp\left\{-\frac{z^2}{4D(t-T)}\right\} + |z|\sqrt{\pi} \left(\operatorname{erf}\left(\frac{|z|}{\sqrt{4Dt}}\right) - \operatorname{erf}\left(\frac{|z|}{\sqrt{4D(t-T)}}\right) \right) \right] \quad (\text{A.10})$$

A limiting case for (A.10) at $t \gg T$ is a 1D-diffusion profile $\propto e^{-z^2/4Dt}$, which can be obtained in a much simpler way by integrating the corresponding limit of (A.9).

B. Cosmic-Ray Diffusion in QLT

B.1. Angular Diffusion Coefficient

A full calculation of the CR diffusion coefficient in QLT can be found in [53]. In this section we show a basic approach that leads to correct functional dependence without a numerical accuracy.

As briefly described in Section 3, to estimate diffusion length, we calculate approximate value at which scattering angle exceeds 1. To do this calculation, we introduce $\mu = v_\eta/v_{\eta 0}$, which equals 1 in the beginning of CR transport process, when particle's guiding center moves along η with $v_{\eta 0} = v_{||}$.

By definition, $D_{\mu\mu} = \frac{\langle \Delta\mu^2 \rangle}{\Delta t}$.

$$\text{In turn, } \Delta\mu^2 = \frac{\Delta v_\eta^2}{v_{||}^2} = \frac{v_\eta^2 - v_{||}^2}{v_{||}^2} = \frac{-(\Delta v_\perp)^2}{v_{||}^2}.$$

The particle moves in a regular magnetic field B_0 with gyration frequency $\Omega_g = \frac{eB_0c}{E}$ and radius $r_g = \frac{v_\perp}{\Omega_g}$, in case $\delta B \ll B_0$, we can apply the guiding center motion description.

Guiding center velocity of the particle experiences a slight change under the action of the Lorentz force in a turbulent vertex with MF δB_k (see Figure 36):

$$\Delta v_\perp = \frac{e\delta B_k c v_{||}}{E} \Delta t = \frac{\delta B_k}{B_0} \Omega_g v_{||} \Delta t. \quad (\text{B.1})$$

From this moment, there are two limiting cases.

Low rigidity case

For a particle with gyration radius $r_g \ll \lambda_c$, the most effective scattering vertices are of scale $k_g \sim 1/r_g$. Such vertices occupy a part of a power-law turbulent spectrum

$$\delta B_k^2 = \delta B^2 \left(\frac{k_g}{k_{\min}} \right)^{-s} \frac{\Delta k}{k_{\min}} \simeq \delta B^2 \left(\frac{r_g}{\lambda_c} \right)^{s-1}.$$

This means that $\Delta v_\perp^2 = \left(\frac{\delta B}{B_0} \right)^2 \left(\frac{r_g}{\lambda_c} \right)^{s-1} \Omega_g^2 v_{||}^2 (\Delta t)^2$.

Thus, $D_{\mu\mu} = \left(\frac{\delta B}{B_0} \right)^2 \left(\frac{r_g}{\lambda_c} \right)^{s-1} \frac{v_\perp^2}{v_{||} r_g}$, where Δt was substituted by $\Delta t = r_g/v_{||}$.

By rearranging the formula, we obtain

$$D_{\mu\mu} = \left(\frac{\delta B}{B_0} \right)^2 \left(\frac{r_g}{\lambda_c} \right)^{s-2} \left(\frac{v_\perp}{v_{||}} \right)^2 \frac{v_{||}}{\lambda_c} \quad (\text{B.2})$$

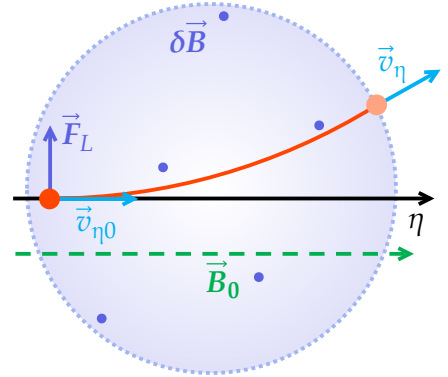


Figure 36: Deviation of a high-energy electron in turbulent magnetic field.

High rigidity case

A particle with gyration radius $r_g \gg \lambda_c$ scatters mostly on the largest-scale turbulent vertices. As $s > 1$ for all turbulence models, it is reasonable to assign all magnetic field energy to the λ_c scale modes. Hence, from (B.1) we simply traverse to $\Delta v_\perp^2 = \left(\frac{\delta B}{B_0}\right)^2 \left(\frac{v_\perp}{r_g}\right)^2 v_\parallel^2 (\Delta t)^2$.

And with $\Delta t = \lambda_c/v_\parallel$, obtain

$$D_{\mu\mu} = \left(\frac{\delta B}{B_0}\right)^2 \left(\frac{r_g}{\lambda_c}\right)^{-2} \left(\frac{v_\perp}{v_\parallel}\right)^2 \frac{v_\parallel}{\lambda_c} \quad (\text{B.3})$$

B.2. Diffusion Length and Parallel Diffusion Coefficient

Ballistic transport changes to diffusive when scattering angle exceeds 1. Thus, one defines *parallel ballistic timescale* τ_\parallel such that $\langle \mu^2 \rangle \sim 1$ or $D_{\mu\mu} \tau_\parallel \sim 1$.

In ballistic regime particle moves with v_\parallel , hence one defines *parallel mean free path* $\lambda_\parallel = v_\parallel \tau_\parallel$. By using (B.2) and (B.3), we write

$$\lambda_\parallel \propto \lambda_c (\cot \alpha)^2 \left(\frac{B_0}{\delta B}\right)^2 \times \begin{cases} (r_g/\lambda_c)^{2-s} \propto (E/B_0)^{2-s}, & r_g \ll \lambda_c, \\ (r_g/\lambda_c)^2 \propto (E/B_0)^2, & r_g \gg \lambda_c. \end{cases} \quad (\text{B.4})$$

Parallel diffusion coefficient is defined by $D_\parallel = \frac{1}{3} c \lambda_\parallel$.

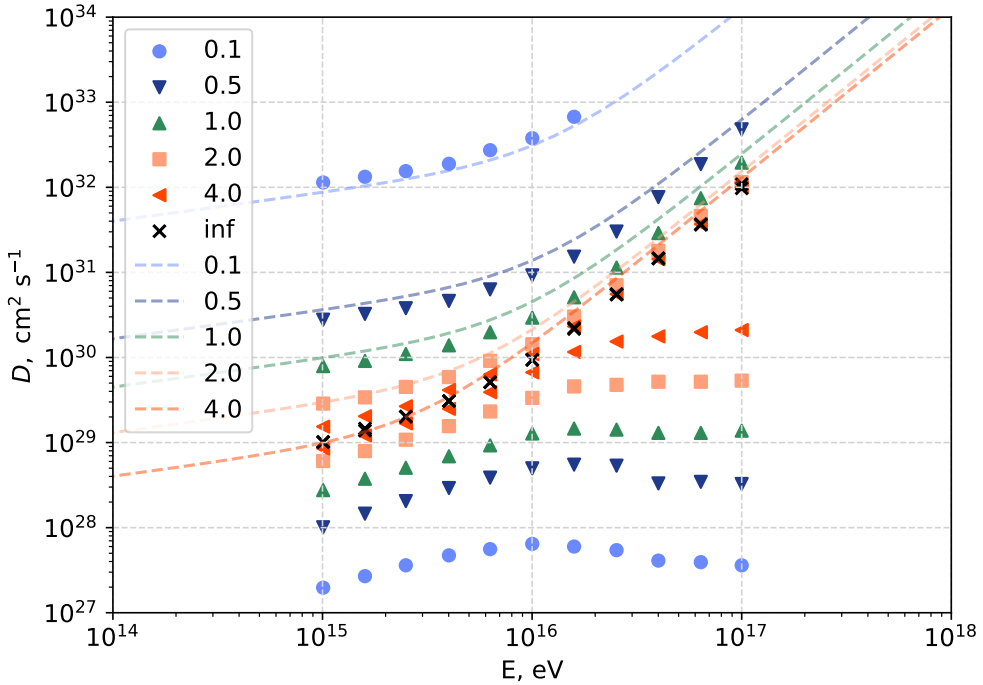


Figure 37: Diffusion coefficient numerical calculation from [52] and QLT approximation.

C. Cosmic-Rays Propagation and Telegrapher's Equation

C.1. A toy-model for particle transport

To construct an equation which tends to reach a diffusive limit at large times, the free transport equations 2.3 have to get a collision term. A straightforward way to add it, is to use the "relaxation time approximation" and write

$$\begin{cases} \frac{\partial n_+}{\partial t} + v \frac{\partial n_+}{\partial z} = -\frac{n_+ - n_-}{2\tau} + \frac{1}{2}q(z, t), \\ \frac{\partial n_-}{\partial t} - v \frac{\partial n_-}{\partial z} = -\frac{n_- - n_+}{2\tau} + \frac{1}{2}q(z, t). \end{cases} \quad (\text{C.1})$$

Here we assume, that collision term is the stronger, the higher is the difference between particles moving along and against the z -axis (regular field direction). This assumption does not account for complicated physics of particle scattering and mirroring in regular-turbulent magnetic field configuration, but substitutes this interaction in the simplest non-trivial way.

By introducing total density $n = n_+ + n_-$ and particle flux $j = j_+ + j_- = v(n_+ - n_-)$, we obtain

$$\begin{cases} \frac{\partial n}{\partial t} + \frac{\partial j}{\partial z} = q, \\ \frac{\partial j}{\partial t} + \frac{j}{\tau} = -v^2 \frac{\partial n}{\partial z}, \end{cases} \quad (\text{C.2})$$

which can be transformed to a second-order equation for n and an expression j :

$$\begin{cases} \frac{\partial^2 n}{\partial t^2} + \frac{1}{\tau} \frac{\partial n}{\partial t} - v^2 \frac{\partial^2 n}{\partial z^2} = \frac{\partial q}{\partial t} + \frac{q}{\tau}, \\ j(z, t) = -v^2 e^{-\frac{t}{\tau}} \int_{-\infty}^t \frac{\partial n}{\partial z}(z, t') e^{\frac{t'}{\tau}} dt'. \end{cases} \quad (\text{C.3})$$

The first equation in (C.3) is known as *telegrapher's equation* and is used in circuit theory and relativistic thermodynamics [72, 73].

One can see that at times $t \ll \tau$ the terms with $1/\tau$ factor are negligible, which causes the first equation to become a free-propagation wave-equation (2.5).

In the opposite limit of $t \gg \tau$, the first line in (C.3) reduces to diffusion equation $\frac{\partial n}{\partial t} - v^2 \tau \frac{\partial^2 n}{\partial z^2} = q$ with $D = v^2 \tau$.

C.2. Green's function for one-dimensional telegrapher's equation

Causal Green's function for telegrapher's equation can be found in [73] (see eqs. (7.4.18) – (7.4.27)). In notation of (C.3), it is written as

$$G(z, t) = \frac{1}{2v} e^{-\frac{t}{2\tau}} J_0 \left[\frac{1}{2v\tau} \sqrt{z^2 - (vt)^2} \right] \mathbf{1}(vt \geq |z|),$$

where $J_0(\zeta)$ denotes Bessel function of the first kind.

The indicator function $\mathbf{1}(vt \geq |z|)$ constraints propagation velocity to be $\leq v$. This also makes the argument of Bessel function purely imaginary, which allows rewriting the Green's function with

the use of the *modified Bessel function* $I_0(\xi) = J_0(i\xi)$. Thus, we rewrite

$$G(z, t) = \frac{1}{2\nu} e^{-\frac{t}{2\tau}} I_0 \left[\frac{t}{2\tau} \sqrt{1 - \left(\frac{z}{vt} \right)^2} \right] \mathbf{1}(vt \geq |z|). \quad (\text{C.4})$$

Solution of the telegrapher's equation in form (C.3) can be found as

$$n(z, t) = \int_{-\infty}^z dz' \int_{-\infty}^t dt' G(z - z', t - t') \left(\frac{\partial q}{\partial t}(z', t') + \frac{q(z', t')}{\tau} \right),$$

which can be transformed via partial integration into (C.2) with a modified Green's function $\tilde{G}(z, t)$.

$$\begin{aligned} n(z, t) &= \int_{-\infty}^z dz' \int_{-\infty}^t dt' \tilde{G}(z - z', t - t') q(z', t'), \text{ where} \\ \tilde{G}(z, t) &= \frac{1}{4\nu\tau} e^{-\frac{t}{2\tau}} \left(2\nu\tau \delta(vt - |z|) + I_0 \left[\frac{t}{2\tau} \sqrt{1 - \left(\frac{z}{vt} \right)^2} \right] + \frac{vt}{\sqrt{(vt)^2 - z^2}} I_1 \left[\frac{t}{2\tau} \sqrt{1 - \left(\frac{z}{vt} \right)^2} \right] \right) \mathbf{1}(vt \geq |z|). \end{aligned} \quad (\text{C.5})$$

Limiting cases

- As already mentioned before, the limit $t \ll \tau$ should lead us to a free propagation Green's function. As for $\xi \rightarrow 0$, $I_0(\xi) \rightarrow 1$, $I_1(\xi) \rightarrow \xi/2$ [74], we indeed recover (2.6).

$$\tilde{G}(z, t \ll \tau) \simeq \frac{1}{4\nu\tau} e^{-t/2\tau} (2\nu\tau \delta(vt - |z|) + O(1) + O(t/\tau)) \simeq \frac{1}{2} \delta(vt - |z|).$$

- Diffusion limit is slightly more technical. Independent of index ν , the leading order asymptotic behavior of the modified Bessel function is $I_\nu(\xi) \simeq e^\xi / \sqrt{2\pi\xi}$ [74].

The argument $\frac{t}{2\tau} \sqrt{1 - (z/vt)^2} \simeq \frac{t}{2\tau} - \frac{1}{2} \frac{z^2}{2\nu^2\tau t}$. The delta-term is exponentially suppressed, the term in front of $I_1(\xi)$ is close to 1. Thus, we are left with the diffusion Green's function with $D = \nu^2\tau$.

$$\tilde{G}(z, t \gg \tau) \simeq \frac{1}{4\nu\tau} \frac{1}{\sqrt{\pi t/\tau}} e^{-t/2\tau} \left(2e^{\frac{t}{2\tau} - \frac{1}{2} \frac{z^2}{4\nu^2\tau t}} \right) = \frac{1}{\sqrt{4\pi\nu^2\tau t}} e^{-\frac{z^2}{4\nu^2\tau t}}.$$

C.3. Artificial Green's function for three-dimensional case

The particles flying out of the source initially orient along the regular field B_0 aligned with z -axis, hence we use a one-telegrapher's equation along z to describe the particle distribution.

Nevertheless, the turbulent magnetic field accounts not only for particles mirroring (which leads to longitudinal diffusion), but also to scattering, causing the particles to diffuse in orthogonal direction. To account for this effect, we multiply the 1D Green's function (C.2) by the 2D-diffusion GF

$$g_2(r_\perp, t) = \frac{1}{4\pi D_\perp t} e^{-\frac{r_\perp^2}{4D_\perp t}}, \text{ where } r_\perp = \sqrt{x^2 + y^2}.$$

Thus, the 3D Green's function is $G(x, y, z, t) = \tilde{G}(z, t) \times g_2(r_\perp, t)$.

D. Solving the Transport Equation

D.1. Method of characteristics

To describe the changing spectrum of particles, which experience energy losses, one uses *the transport equation* [2]. A minimally general form for the problem of our interest can be written as a conservation-law (D.1) or in an expanded form (D.2).

$$\frac{\partial N}{\partial t}(E, t) + \frac{\partial}{\partial E} (\dot{E}(E)N(E, t)) = Q(E, t). \quad (\text{D.1})$$

$$\frac{\partial N}{\partial t}(E, t) + \dot{E}(E) \frac{\partial N}{\partial E}(E, t) = -\frac{\partial \dot{E}}{\partial E}(E)N(E, t) + Q(E, t). \quad (\text{D.2})$$

Here we choose the time t_0 that passed since the ejection started and its rate $Q(E, t)$. The final energy distribution is observed at $t = 0$. We assume there was no particles at $t < -t_0$.

Equation (D.1) is a first-order hyperbolic partial derivative equation, hence it can be solved with the use of the *method of characteristics* [71]. The idea behind this approach is to find a family of lines $\{\gamma = \gamma(s)\}_{s \in \mathbb{R}}$, along which D.1 reduces to an ordinary differential equation (ODE). In other words, along these lines we have

$$\frac{d}{ds}N(E(s), t(s)) = F(E(s), t(s), N(s)). \quad (\text{D.3})$$

By expanding the left-hand part in (D.3), we get

$$\frac{d}{ds}N(E(s), t(s)) = \frac{\partial N}{\partial t} \frac{dt}{ds} + \frac{\partial N}{\partial E} \frac{dE}{ds}.$$

Direct comparison to (D.2) suggests setting $s \equiv t$ to get $dt/ds \equiv 1$ and leads to energy evolution equation, which defines a family of characteristics

$$\frac{dE}{dt} = \dot{E}(E(t)). \quad (\text{D.4})$$

A single characteristic $\gamma(t|E_0)$ can be chosen by implying an initial condition $E|_{t=0} = E_0$ for energy in the final state at $t = 0$. With $f(t) = \frac{\partial \dot{E}}{\partial E}(E(t|E_0))$, for each line one gets an ODE

$$\frac{dN}{dt}(t) = -f(t)N(t) + Q(t),$$

which has the following solution for each E_0

$$N(t) = N(t_1) \exp \left\{ - \int_{t_1}^t dt' f(t') \right\} + \int_{t_1}^t dt' Q(t') \exp \left\{ - \int_{t'}^t dt'' f(t'') \right\}.$$

To conclude, we write the result of our interest with $t_1 = -t_0$ and $t = 0$:

$$N(E_0) = \int_{-t_0}^0 dt' Q(E(t'|E_0), t') \exp \left\{ - \int_{t'}^0 dt'' \frac{\partial \dot{E}}{\partial E}(E(t''|E_0)) \right\} \quad (\text{D.5})$$

D.2. Analytical solution for power-law losses

If the energy-loss function $\dot{E}(E)$ is an energy power-law, as seen for synchrotron losses and IC scattering in Thomson regime, integral (D.5) can be simplified. Assume

$$\dot{E}(E) = -aE^p, \quad \frac{\partial \dot{E}}{\partial E}(E) = -apE^{p-1}. \quad (\text{D.6})$$

Then the backpropagation equation (D.4) can be solved explicitly (remember that $t < 0$):

$$\begin{aligned} \frac{dE}{dt} = -aE^p &\Leftrightarrow \int_E^{E_0} \frac{dE}{E^{p-1}} = -a \int_{t'}^0 dt' \Leftrightarrow E_0^{-p+1} = E^{-p+1} + a(p-1)(-t) \\ \text{or } E_0^{p-1} &= \frac{E^{p-1}}{1 - a(p-1)tE^{p-1}}, \text{ and } E^{p-1} = \frac{E_0^{p-1}}{1 + a(p-1)tE_0^{p-1}}. \end{aligned} \quad (\text{D.7})$$

The integral under exponent is also done analytically:

$$-\int_{t'}^0 dt'' \frac{\partial \dot{E}}{\partial E}(E(t''|E_0)) = ap \int_{t'}^0 dt'' E^{p-1}(t''|E_0) = -\frac{p}{p-1} \ln \left(1 + a(p-1)t'E_0^{p-1} \right).$$

This finally leads us to an analytical result for power-law losses:

$$N(E_0) = \int_{-t_0}^0 dt' Q(E(t'|E_0), t') \left(1 + a(p-1)t'E_0^{p-1} \right)^{-\frac{p}{p-1}}. \quad (\text{D.8})$$

Case $p = 2$

For synchrotron and Thomson limit of Inverse Compton losses $p = 2$. In this case

$$N(E, t) = \int_{-t_0}^0 dt' Q \left(\frac{E_0}{1 + aE_0 t'}, t' \right) \left(\frac{1}{1 + aE_0 t'} \right)^2 \quad (\text{D.9})$$

The two families of characteristics are demonstrated in Figure 38.

One can notice that each emission time $t' < 0$ has a corresponding maximum energy $E_{\max} = (a|t'|)^{-1}$, i.e. the particles ejected at t' by the moment of observation have been already cooled to $E < E_{\max}(t')$.

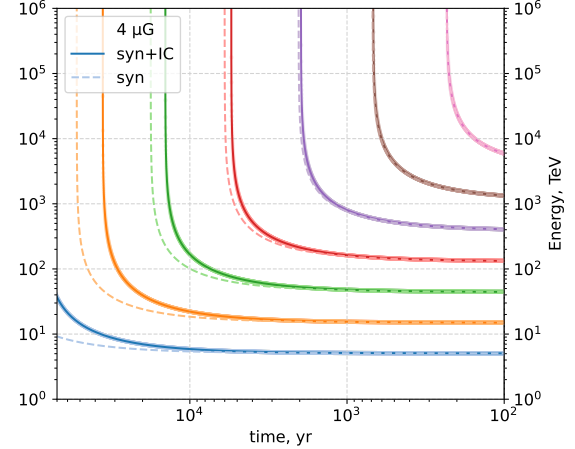


Figure 38: Characteristics for single synchrotron cooling (dashed) and synchrotron cooling with the Inverse Compton contribution (solid) for different final energies.

D.3. Limiting cases

Single Ejection Scenario

The single ejection scenario corresponds to a delta-like release of particles at $-t_0$

$$Q(E, t) = N_0(E)\delta(t + t_0).$$

Substitution into (D.5) allows to remove outer integral and write

$$N(E_0) = N_0(E(-t_0|E_0)) \exp\left\{-\int_{-t_0}^0 dt'' \frac{\partial \dot{E}}{\partial E}(E(t''|E_0))\right\}. \quad (\text{D.10})$$

In the power-law losses case, the expression (D.8) becomes fully analytical:

$$N(E_0) = N_0\left(\left(\frac{E_0^{p-1}}{1 - a(p-1)t_0 E_0^{p-1}}\right)^{\frac{1}{p-1}}\right)\left(1 - a(p-1)t_0 E_0^{p-1}\right)^{-\frac{p}{p-1}}. \quad (\text{D.11})$$

With $p = 2$, (D.11) can be significantly simplified:

$$N(E_0) = N_0\left(\frac{1}{1 - aE_0 t_0}\right)\left(\frac{1}{1 - aE_0 t_0}\right)^2. \quad (\text{D.12})$$

Again, there is a maximal final energy value $E_0 = (at_0)^{-1}$ due to synchrotron (IC) losses.

Steady-State Emission Scenario

A steady-state scenario corresponds to a time-independent constant particle emission for an amount of time much larger than corresponding cooling timescales. In this case, the number of particles time variation is negligible, and (D.1) transforms into

$$\frac{\partial}{\partial E}(\dot{E}(E)N(E)) = Q(E). \quad (\text{D.13})$$

To obtain a solution, we integrate the ejection term and write

$$N(E_0) = -\frac{1}{\dot{E}(E_0)} \int_{E_0}^{+\infty} dE Q(E). \quad (\text{D.14})$$

For power-law losses $\dot{E} = -aE^p$, and injection spectrum $Q(E) = qE^{-s}$, we get a softer power-law in the final state:

$$N(E_0) = \frac{q}{a(s-1)} E^{-s+1-p}. \quad (\text{D.15})$$

Thus, in case $p = 2$, we recover the famous result

$$N(E_0) = \frac{q}{a} E^{-(p+1)}, \quad (\text{D.16})$$

which means that for synchrotron (IC) losses, the final spectrum is one order steeper than the injected one.

D.4. Matrix-based numerical approach

As we are working with MCMC simulations, we need a fast and reliable method to calculate the spectra.

In terms of calculations on a grid, we can rewrite (D.5) as

$$N(E_i) = \int_{-t_0}^0 dt' Q(E_i, t') \Phi(E_i, t'), \quad (\text{D.17})$$

where $Q(E_i, t') = Q(E(t'|E_i), t')$, $\Phi(E_i, t') = \exp \left\{ - \int_{t'}^0 dt'' \frac{\partial \dot{E}}{\partial E}(E(t''|E_i)) \right\}$

As backpropagation and function Φ do not depend on the ejection rate, these values can be precomputed on a given time-energy grid for each energy-loss model. Thus, to solve the equation we proceed as follows:

1. Establish a time-energy grid $(E_i, t_j) \in [E_{\min}, E_{\max}] \times [-T_0, 0]$.
2. Propagate back each final energy E_i by solving (D.4) and obtain a matrix $\mathcal{E}_{ij} = E(t_j|E_i)$.
3. Calculate the 'modulation coefficient' matrix Φ_{ij} exponentiating backward cumulative integral of the energy loss derivative.
4. Compute the injection matrix $Q_{ij} = Q(\mathcal{E}_{ij}, t_j)$.
5. By numerical integration for a given $t_0 \in [0, T_0]$ calculate the final spectrum.

E. Inverse Compton and Synchrotron Radiation

This and several other appendix sections remain to be completed.

F. Cold proton density and hadronic emission

This and several other appendix sections remain to be completed.

G. Rescaling XRISM X-ray measurements

This and several other appendix sections remain to be completed.

H. Measuring orthogonal diffusion coefficient

This and several other appendix sections remain to be completed.

Appendix References

- [2] Longair, M.S. *High Energy Astrophysics*. Cambridge: Cambridge University Press, Feb. 2011.
- [6] Olivera-Nieto, L. “H.E.S.S. detection of very high energy emission surrounding the micro-quasar V4641 Sgr”. 2024.
- [52] Giacinti, G., Kachelriess, M., and Semikoz, D.V. “Reconciling cosmic ray diffusion with Galactic magnetic field models”. *J. Cosmol. Astropart. Phys.* 2018.07 (July 2018), pp. 051–051.
- [53] Shalchi, A. *Nonlinear Cosmic Ray Diffusion Theories*. Vol. 362. 2009. Chap. 2 and 3. [DOI](#).
- [71] Tikhonov, A.N. and Samarskii, A.A. *Equations of Mathematical Physics*. Russian. 6th, revised and expanded. Moscow State University Press, 1999. Chap. 6.
- [72] Koshlyakov, N.S., Gliner, E.B., and Smirnov, M.M. *Partial Differential Equations of Mathematical Physics*. Russian. Moscow: Vysshaya Shkola, 1970.
- [73] Morse, P.M. and Feshbach, H. *Methods of theoretical physics: Pt. 1*. Pure & Applied Physics S. New York, NY: McGraw-Hill, Jan. 1953.
- [74] *NIST Digital Library of Mathematical Functions*. <https://dlmf.nist.gov/>, Release 1.2.4 of 2025-03-15. F. W. J. Olver, A. B. Olde Daalhuis, D. W. Lozier, B. I. Schneider, R. F. Boisvert, C. W. Clark, B. R. Miller, B. V. Saunders, H. S. Cohl, and M. A. McClain, eds. [link](#).